Supplementary Information (SI) for Journal of Materials Chemistry A.
This journal is © The Royal Society of Chemistry 2025

SI

Plasmonic copper nanoparticle aggregates for near-infrared light-driven hydrogen evolution

Qiufen Wang [a], Jie Wang[a]*, Hongxia Zhang [a], Jianghong Zhao[a]*, Hu Shi [a, b]*, and Pengju Yang[a]*

[a]School of Chemistry and Chemical Engineering, Shanxi University, 030006, Taiyuan, China.

[b]Institute of Molecular Science, Shanxi University, 030006, Taiyuan, China.

Content:

Figure S1. Size distribution of Cu NP aggregates.

Figure S2. Orbital interaction diagram for dimer. Vertical axis shows MO energies in eV. Blue solid and dashed bars correspond to occupied and unoccupied MOs, respectively. The MOs are plotted as isosurface graphs with isovalue of 0.01 a.u. Blank texts mark orbital indices. Red texts indicate major contribution of MOs from the monomer A and B to the MOs of dimer. The orbital compositions were evaluated by Mulliken method.

Figure S3. Orbital interaction diagram for tetramer. Vertical axis shows MO energies in eV. Blue solid and dashed bars correspond to occupied and unoccupied MOs, respectively. The MOs are plotted as isosurface graphs with isovalue of 0.01 a.u. Blank texts mark orbital indices. Red texts indicate major contribution of MOs from the dimer A and B to the MOs of tetramer. The orbital compositions were evaluated by Mulliken method.

Figure S4. Electrostatic potential distribution of Cu NP monomer.

Figure S5. The dipole moment values and electrostatic potential distribution were calculated for Cu NP dimers with different structures.

Figure S6. The dipole moment values and electrostatic potential distribution were calculated for Cu NP trimers with different structures.

Figure S7. The dipole moment values and electrostatic potential distribution were calculated for Cu NP tetramers with different structures.

Figure S8. PL spectra of Cu NPs solution with different concentrations.

Figure S9. The PL lifetime of Cu NP monomer (0.005 mg/mL Cu NPs solution) and Cu NP aggregates (0.6 mg/mL Cu NPs solution).

Figure S10. Electron and hole distributions of S0 → S1 (green represents the electron distribution and blue represents the hole distribution) and the exciton binding energy were calculated for the different Cu NP aggregates.

Figure S11. (a) TDM diagram of Cu NP monomer. (b) Electron and hole distributions of Cu NP monomer.

Figure S12. Photocatalytic hydrogen production activities of Cu NP aggregates with different Cu NP concentrations (3 h reaction).

Figure S13. Hydrogen production by 0.6 mg/mL Cu NPs under 450 nm irradiation without Pt.

Figure S14. Hydrogen evolution activity of 0.6 mg/mL Cu NPs at 450 nm in the absence of both Pt and triethylamine.

Figure S15. Photocatalytic hydrogen evolution activity of Cu NPs at different concentrations under 450 nm irradiation.

Figure S16. Effect of temperature on the photocatalytic hydrogen evolution activity of Cu NPs (0.6 mg/mL) under 450 nm irradiation.

Figure S17. Photocatalytic hydrogen evolution activity of Cu NPs (0.6 mg/mL) at 450 nm under different light intensities.

Figure S18. IGMH analysis of boracic acid-modified Cu NP dimer.

Figure S19. IGMH analysis of boracic acid-modified Cu NP trimer.

Figure S20. The dipole moment values and electrostatic potential distribution were calculated for boracic acid-modified Cu NPs with different degrees of aggregation.

Figure S21. Electron and hole distributions of S0 → S1 (green represents the electron distribution and blue represents the hole distribution) and the exciton binding energy were calculated for boracic acid-modified Cu NPs with different degrees of aggregation.

Figure S22. Wavelength-dependent AQY of Cu NP aggregates.

Figure S23. IGMH analysis of 2-methylimidazole-modified Cu NP dimer.

Figure S24. IGMH analysis of 2-methylimidazole-modified Cu NP trimer.

Figure S25. IGMH analysis of 2-methylimidazole-modified Cu NP tetramer.

Figure S26. IGMH analysis of cyclohexane-modified Cu NP dimer.

Figure S27. IGMH analysis of cyclohexane-modified Cu NP trimer.

Figure S28. IGMH analysis of cyclohexane-modified Cu NP tetramer.

Figure S29. IGMH analysis of dimethyl sulfoxide-modified Cu NP dimer.

Figure S30. IGMH analysis of dimethyl sulfoxide-modified Cu NP trimer.

Figure S31. IGMH analysis of dimethyl sulfoxide-modified Cu NP tetramer.

Figure S32. UV-vis absorption spectra of Cu NP aggregates and Cu NP aggregates after adding different compounds (2-methylimidazole, cyclohexane and dimethyl sulfoxide).

Figure S33. The dipole moment values and electrostatic potential distribution were calculated for 2-methylimidazole-modified Cu NPs with different degrees of aggregation.

Figure S34. The dipole moment values and electrostatic potential distribution were calculated for cyclohexane-modified Cu NPs with different degrees of aggregation.

Figure S35. The dipole moment values and electrostatic potential distribution were calculated for dimethyl sulfoxide-modified Cu NPs with different degrees of aggregation.

Figure S36. PL spectra of Cu NP aggregates and Cu NP aggregates after adding different compounds (2-methylimidazole, cyclohexane and dimethyl sulfoxide).

Figure S37. The PL lifetime of Cu NP aggregates after addition of 2-methylimidazole.

Figure S38. The PL lifetime of Cu NP aggregates after addition of cyclohexane.

Figure S39. The PL lifetime of Cu NP aggregates after addition of dimethyl sulfoxide.

Figure S40. Electron and hole distributions of S0 → S1 (green represents the electron distribution and blue represents the hole distribution) and the exciton binding energy were calculated for 2-methylimidazole-modified Cu NPs with different degrees of aggregation.

Figure S41. Electron and hole distributions of S0 → S1 (green represents the electron distribution and blue represents the hole distribution) and the exciton binding energy were calculated for cyclohexane-modified Cu NPs with different degrees of aggregation.

Figure S42. Electron and hole distributions of S0 → S1 (green represents the electron distribution and blue represents the hole distribution) and the exciton binding energy were calculated for dimethyl sulfoxide-modified Cu NPs with different degrees of aggregation.

Figure S43. The photocatalytic performance of 2-methylimidazole-modified Cu NPs (0.6 mg/mL) under visible, red, and NIR light irradiation.

Figure S44. The photocatalytic performance of cyclohexane-modified Cu NPs (0.6 mg/mL) under visible, red, and NIR light irradiation.

Figure S45. The photocatalytic performance of dimethyl sulfoxide-modified Cu NPs (0.6 mg/mL) under visible, red, and NIR light irradiation.

Figure S46. IGMH analysis of Ag NP dimer.

Figure S47. IGMH analysis of Ag NP trimer.

Figure S48. Electrostatic potential distribution of Ag NP monomer.

Figure S49. The dipole moments and electrostatic potential distribution were calculated for Ag NP dimers with different structures.

Figure S50. The dipole moments and electrostatic potential distribution were calculated for Ag NP trimers with different structures.

Figure S51. The dipole moments and electrostatic potential distribution were calculated for Ag NP tetramers with different structures.

Figure S52. Electron and hole distributions of S0 → S1 (green represents the electron distribution and blue represents the hole distribution) and the exciton binding energy were calculated for the different Ag NP aggregates.

Figure S53. (a) The photocatalytic performance of Ag NPs (0.002 mg/mL). (b) The photocatalytic performance of Ag NPs (0.02 mg/mL).

Figure S54. UV-vis absorption spectra of Ag NP aggregates and Ag NP aggregates with 2-methylimidazole modification.

Figure S55. PL spectra of Ag NP aggregates and Ag NP aggregates with 2-methylimidazole modification.

Table S1. Key parameters of all LED light sources: wavelength, light intensity, and photon flux.

Table S2. PL lifetimes of Cu NP monomer and Cu NP aggregates.

Table S3. *f*s-TA kinetic parameters of Cu NP monomer and Cu NP aggregates.

Table S4. Comparison of hydrogen photosynthesis activities with state-of-the-art plasmonic photocatalysts under red/NIR light irradiation.

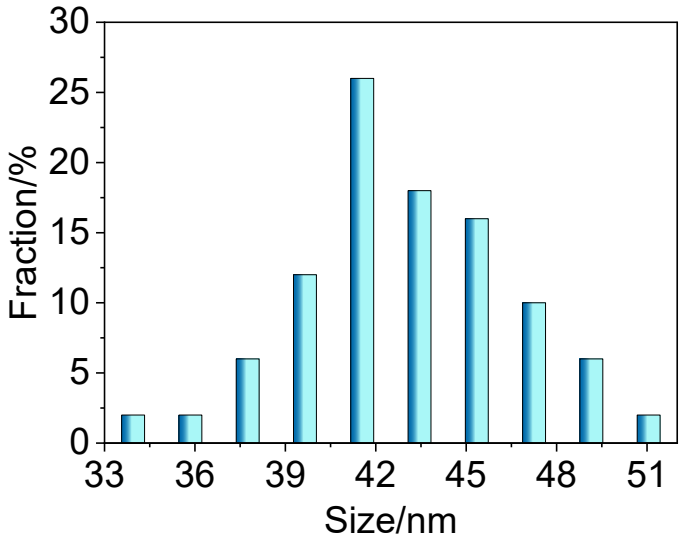

Figure S1. Size distribution of Cu NP aggregates.

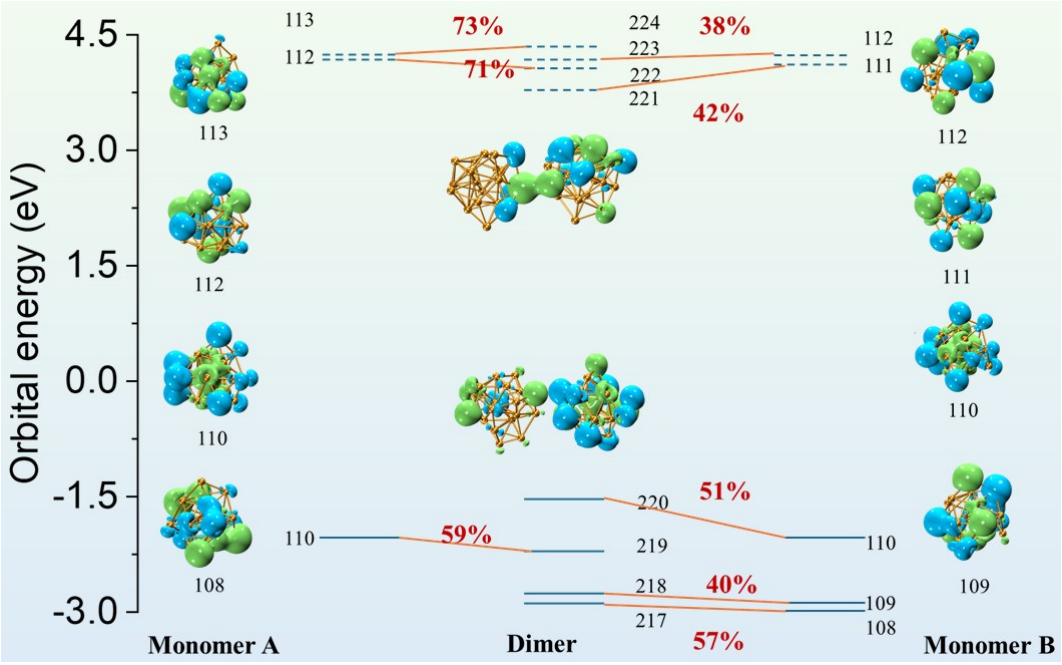

Figure S2. Orbital interaction diagram for dimer. Vertical axis shows MO energies in eV. Blue solid and dashed bars correspond to occupied and unoccupied MOs, respectively. The MOs are plotted as isosurface graphs with isovalue of 0.01 a.u. Blank texts mark orbital indices. Red texts indicate major contribution of MOs from the monomer A and B to the MOs of dimer. The orbital compositions were evaluated by Mulliken method.

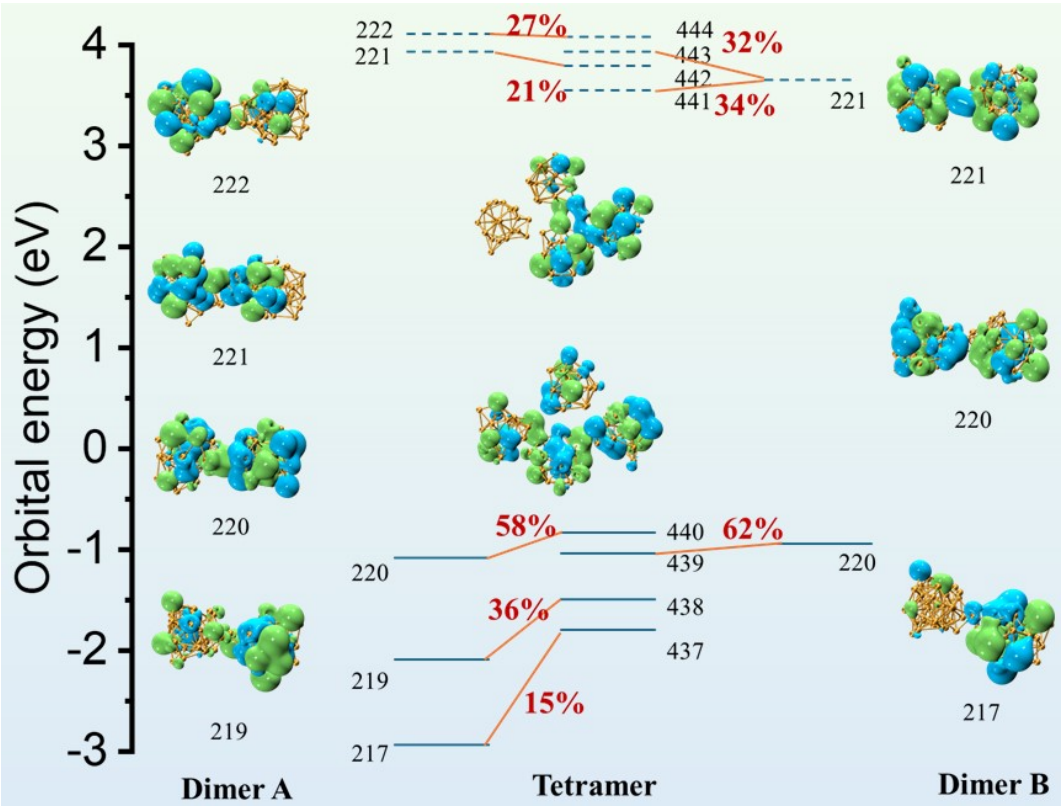

Figure S3. Orbital interaction diagram for tetramer. Vertical axis shows MO energies in eV. Blue solid and dashed bars correspond to occupied and unoccupied MOs, respectively. The MOs are plotted as isosurface graphs with isovalue of 0.01 a.u. Blank texts mark orbital indices. Red texts indicate major contribution of MOs from the dimer A and B to the MOs of tetramer. The orbital compositions were evaluated by Mulliken method.

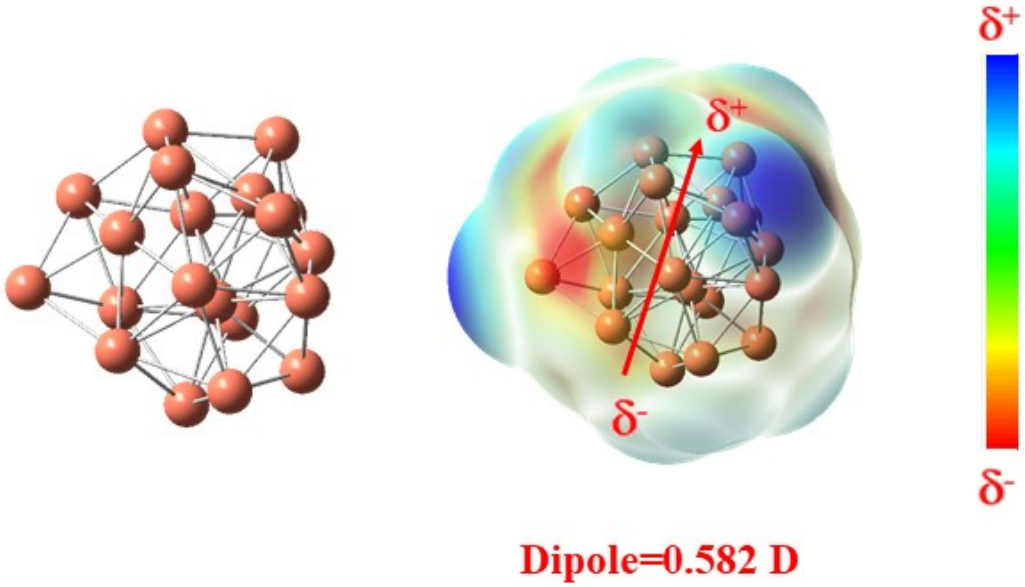

Figure S4. Electrostatic potential distribution of Cu NP monomer.

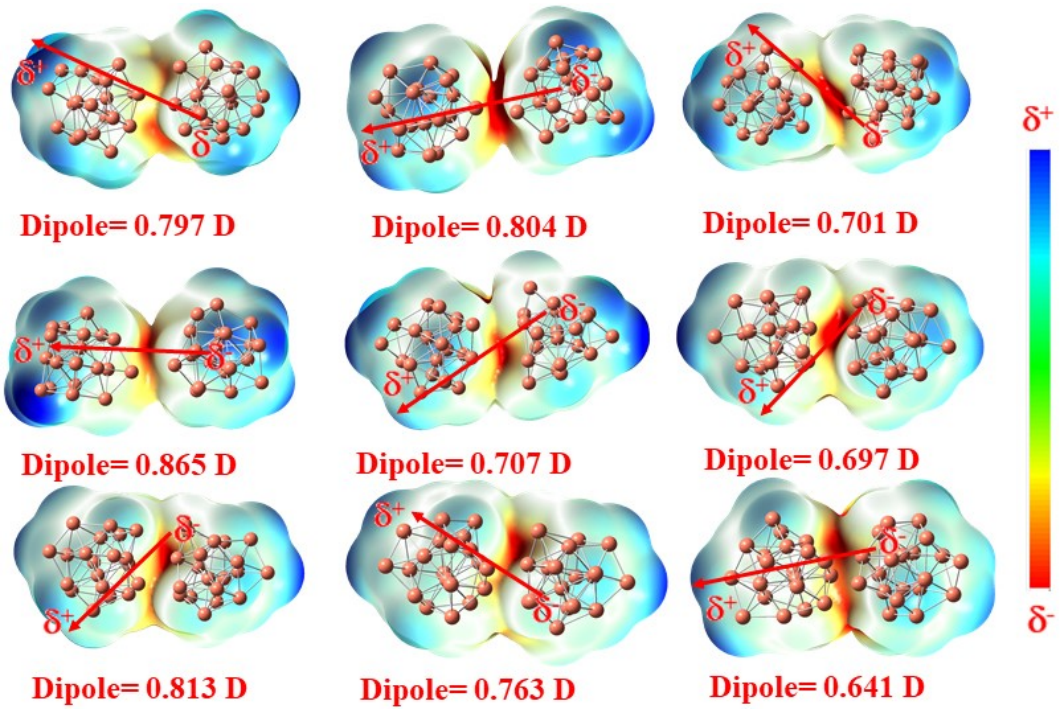

Figure S5. The dipole moment values and electrostatic potential distribution were calculated for Cu NP dimers with different structures.

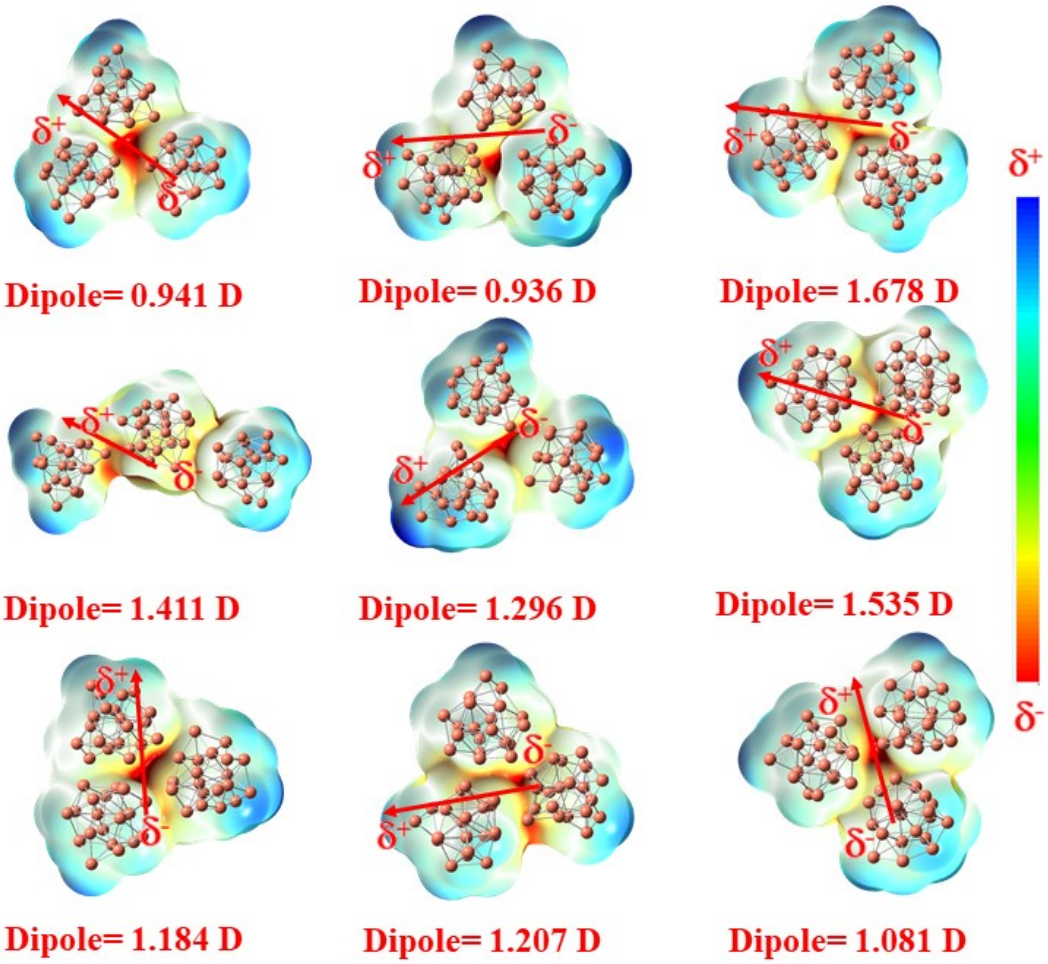

Figure S6. The dipole moment values and electrostatic potential distribution were calculated for Cu NP trimers with different structures.

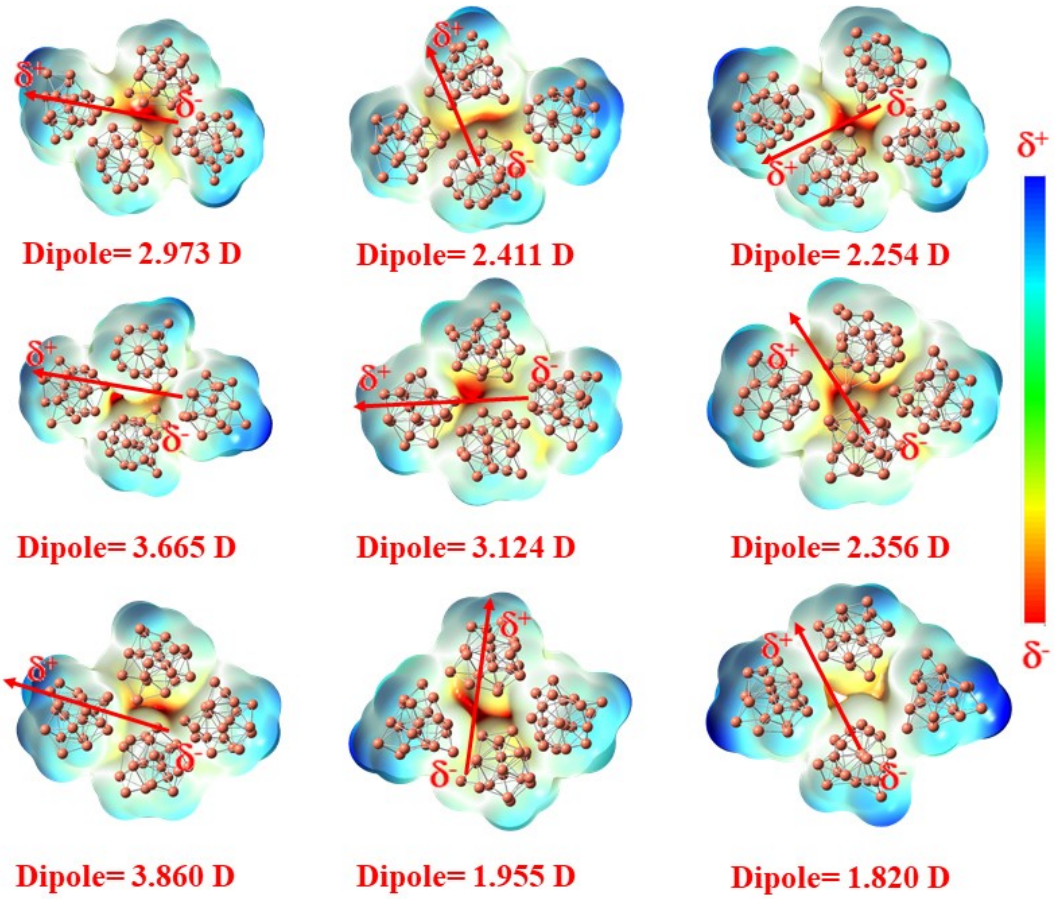

Figure S7. The dipole moment values and electrostatic potential distribution were calculated for Cu NP tetramers with different structures.

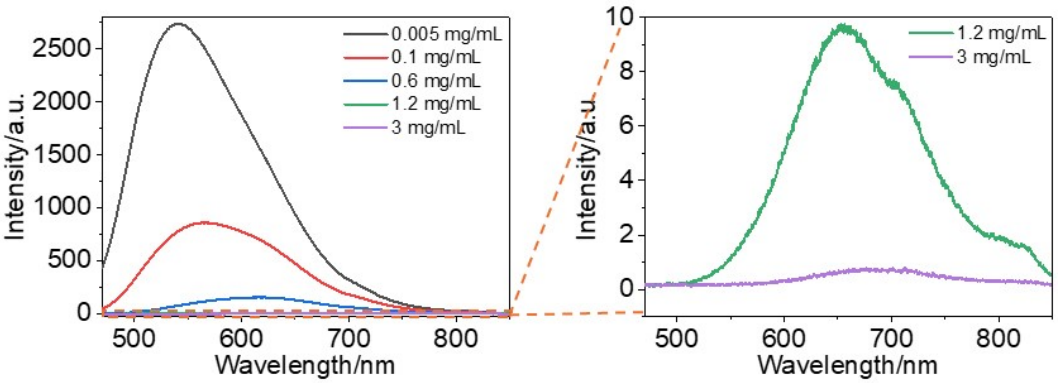

Figure S8. PL spectra of Cu NPs solution with different concentrations.

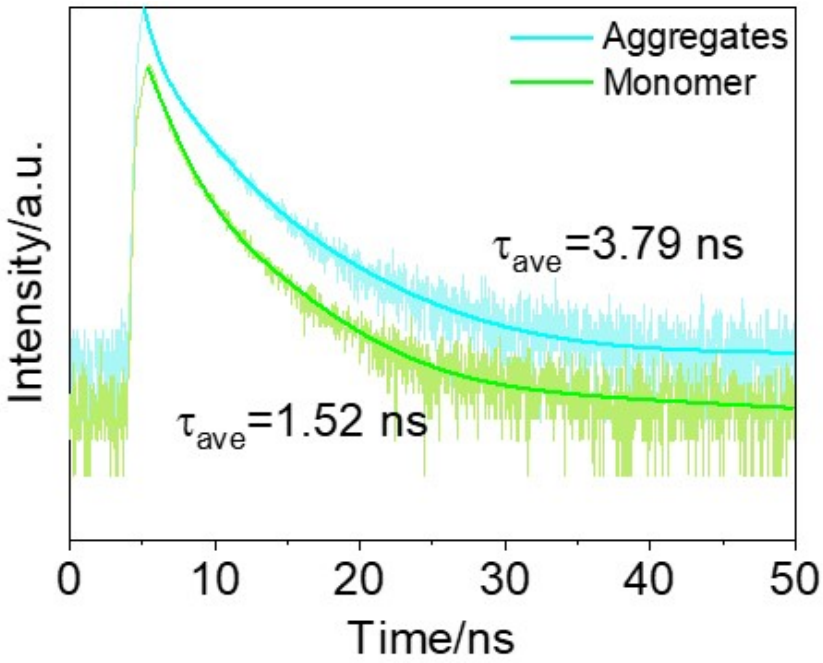

Figure S9. The PL lifetime of Cu NP monomer (0.005 mg/mL Cu NPs solution) and Cu NP aggregates (0.6 mg/mL Cu NPs solution).

	Distribution of electron-hole	The exciton binding energy
Monomer	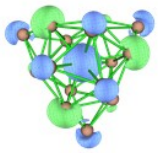	**1.53 eV**
Dimer	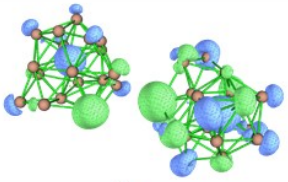	**1.38 eV**
Trimer	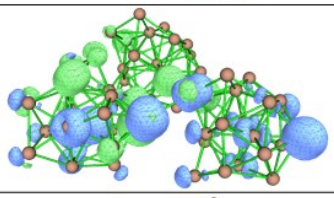	**1.21 eV**
Tetramer	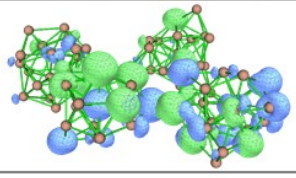	**0.96 eV**

Figure S10. Electron and hole distributions of S0 → S1 (green represents the electron distribution and blue represents the hole distribution) and the exciton binding energy were calculated for the different Cu NP aggregates.

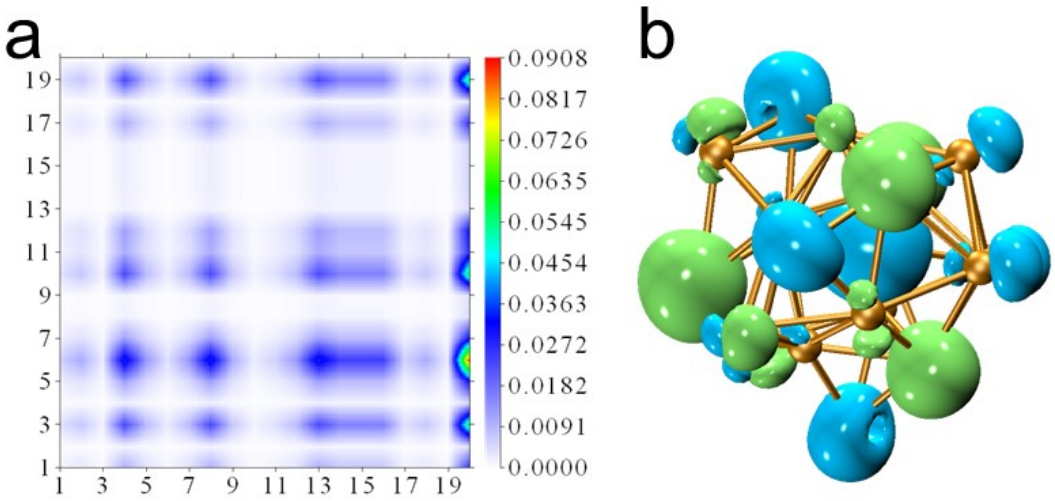

Figure S11. (a) TDM diagram of Cu NP monomer. (b) Electron and hole distributions of Cu NP monomer.

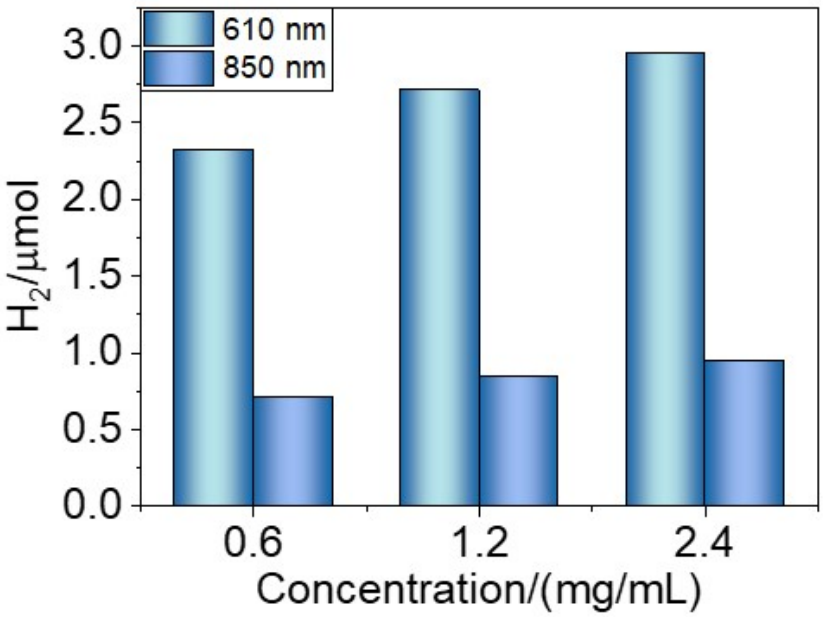

Figure S12. Photocatalytic hydrogen production activities of Cu NP aggregates with different Cu NP concentrations (3 h reaction).

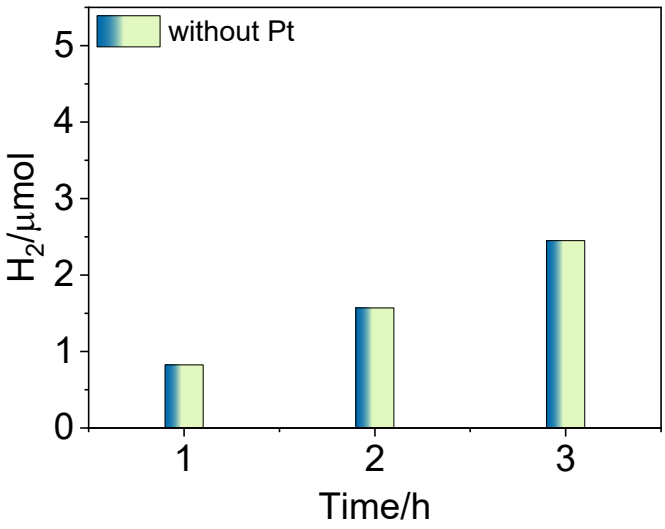

Figure S13. Hydrogen production by 0.6 mg/mL Cu NPs under 450 nm irradiation without Pt.

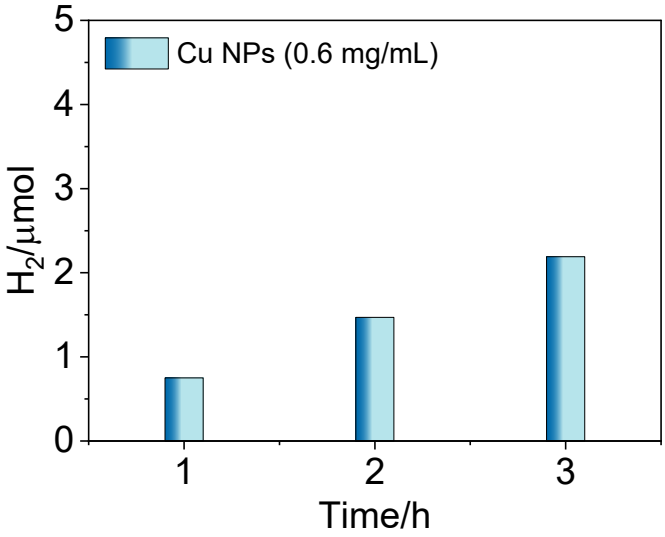

Figure S14. Hydrogen evolution activity of 0.6 mg/mL Cu NPs at 450 nm in the absence of both Pt and triethylamine.

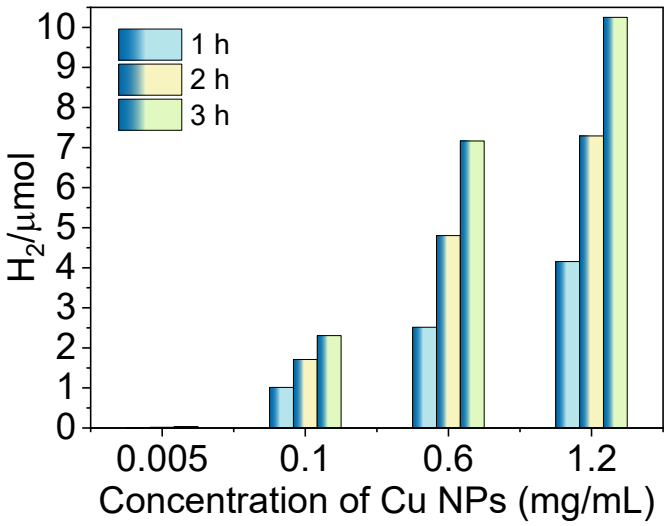

Figure S15. Photocatalytic hydrogen evolution activity of Cu NPs at different concentrations under 450 nm irradiation.

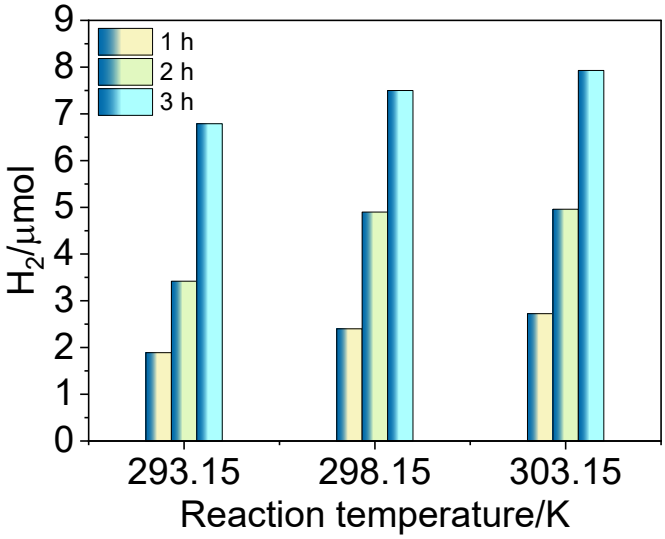

Figure S16. Effect of temperature on the photocatalytic hydrogen evolution activity of Cu NPs (0.6 mg/mL) under 450 nm irradiation.

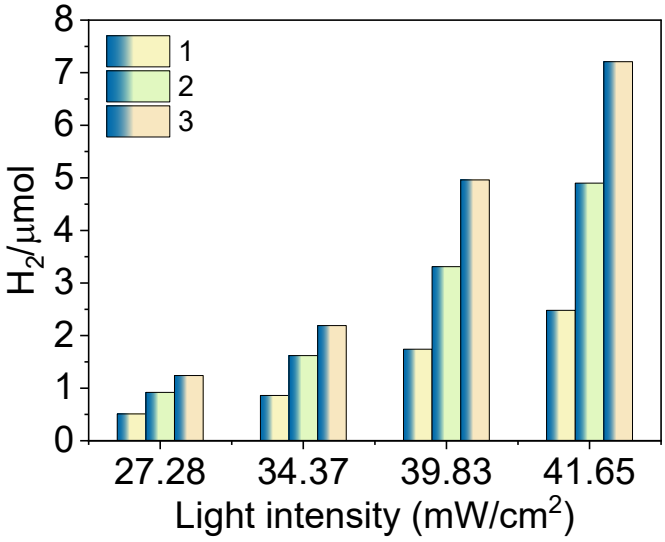

Figure S17. Photocatalytic hydrogen evolution activity of Cu NPs (0.6 mg/mL) at 450 nm under different light intensities.

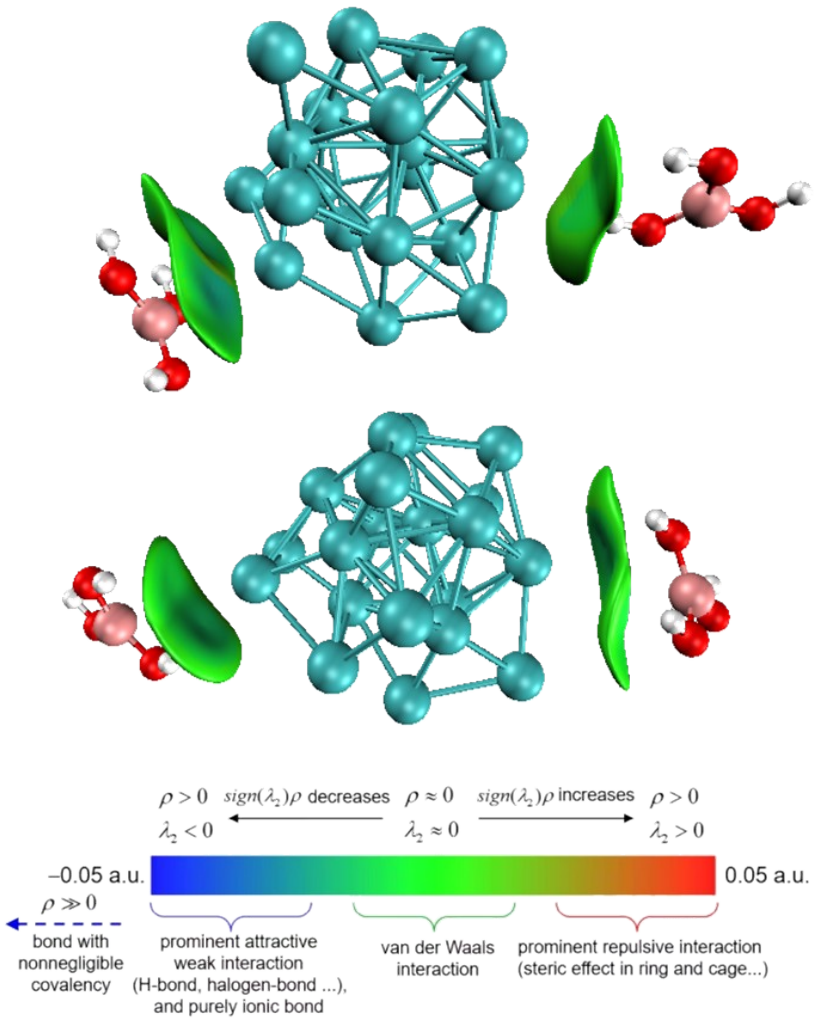

Figure S18. IGMH analysis of boracic acid-modified Cu NP dimer.

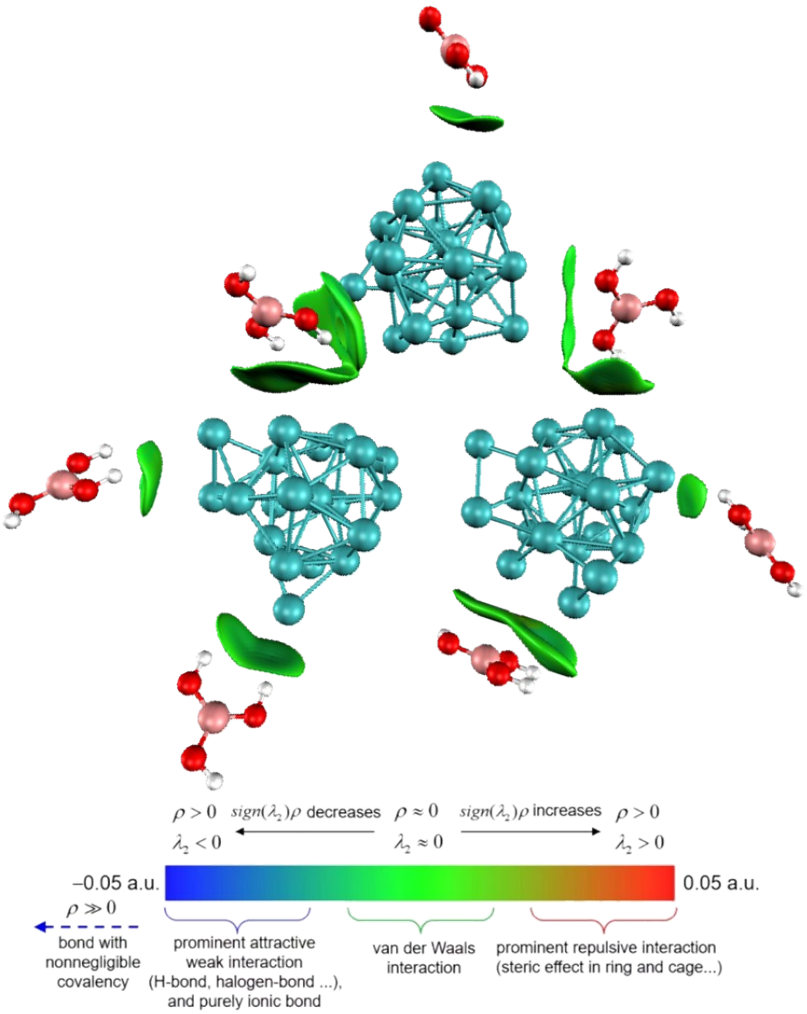

Figure S19. IGMH analysis of boracic acid-modified Cu NP trimer.

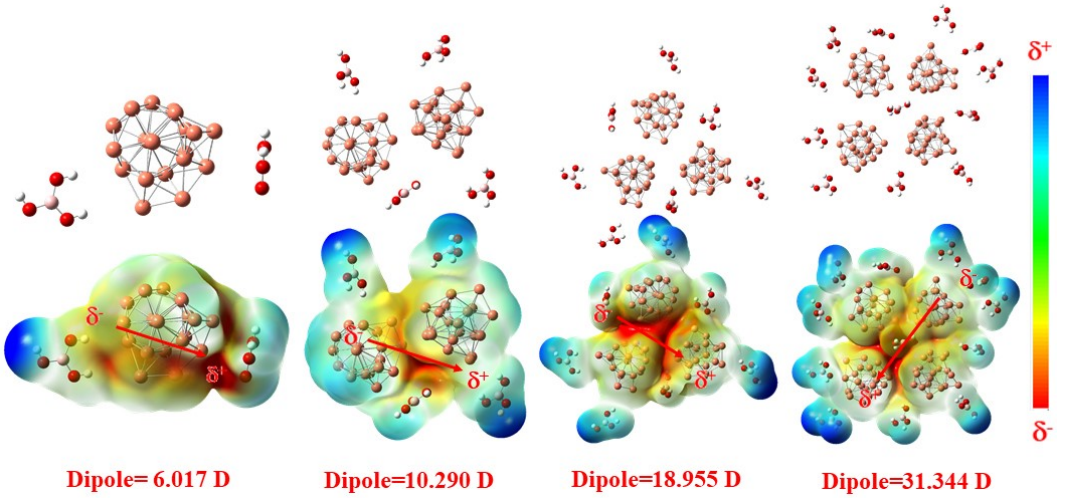

Figure S20. The dipole moment values and electrostatic potential distribution were calculated for boracic acid-modified Cu NPs with different degrees of aggregation.

	Distribution of electron-hole	The exciton binding energy
Dimer	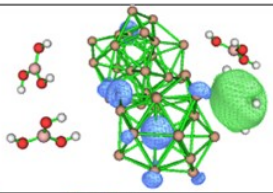	**1.19 eV**
Trimer	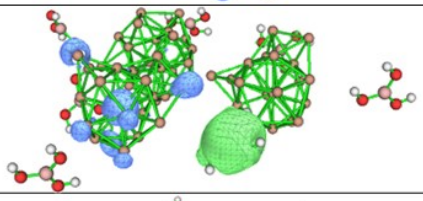	**0.72 eV**
Tetramer	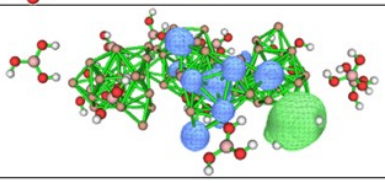	**0.58 eV**

Figure S21. Electron and hole distributions of S0 → S1 (green represents the electron distribution and blue represents the hole distribution) and the exciton binding energy were calculated for boracic acid-modified Cu NPs with different degrees of aggregation.

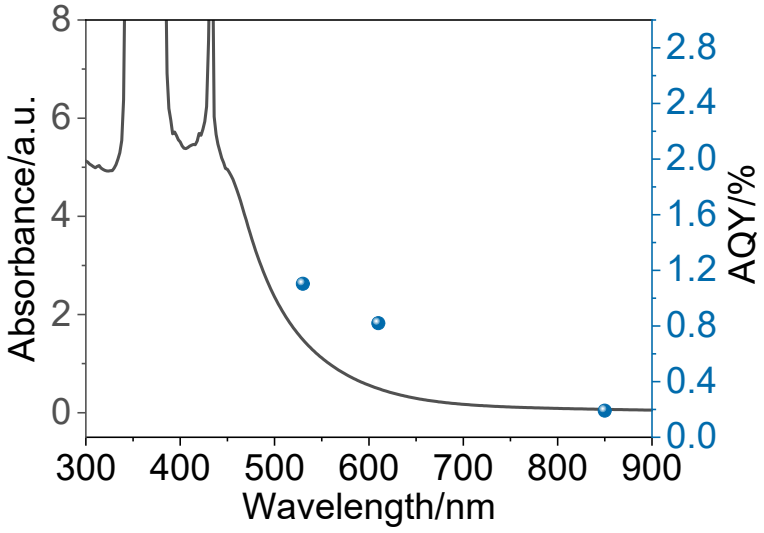

Figure S22. Wavelength-dependent AQY of Cu NP aggregates.

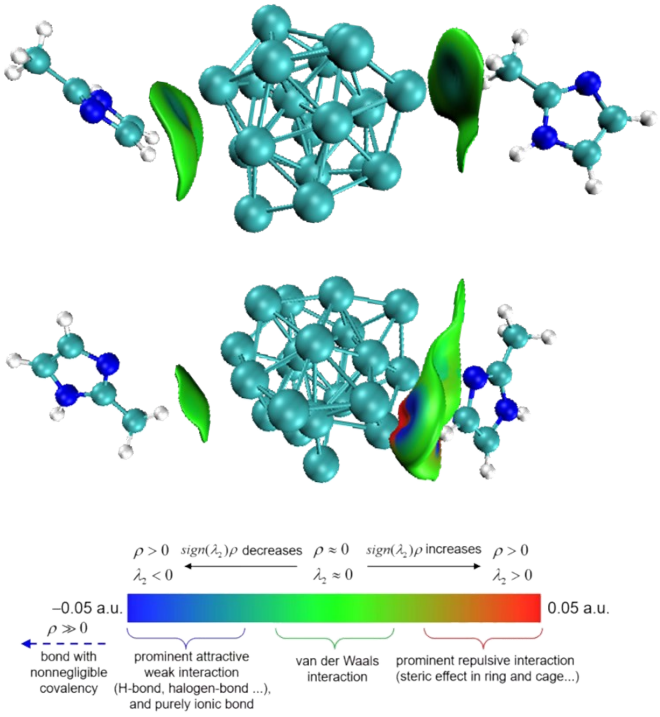

Figure S23. IGMH analysis of 2-methylimidazole-modified Cu NP dimer.

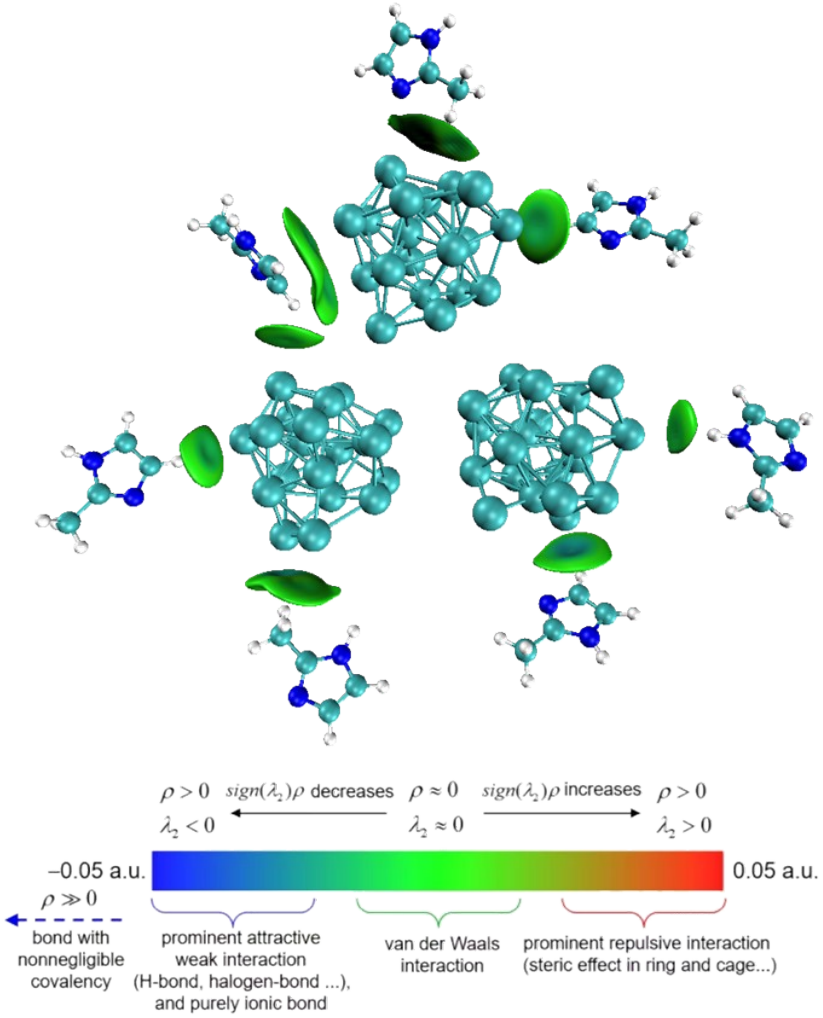

Figure S24. IGMH analysis of 2-methylimidazole-modified Cu NP trimer.

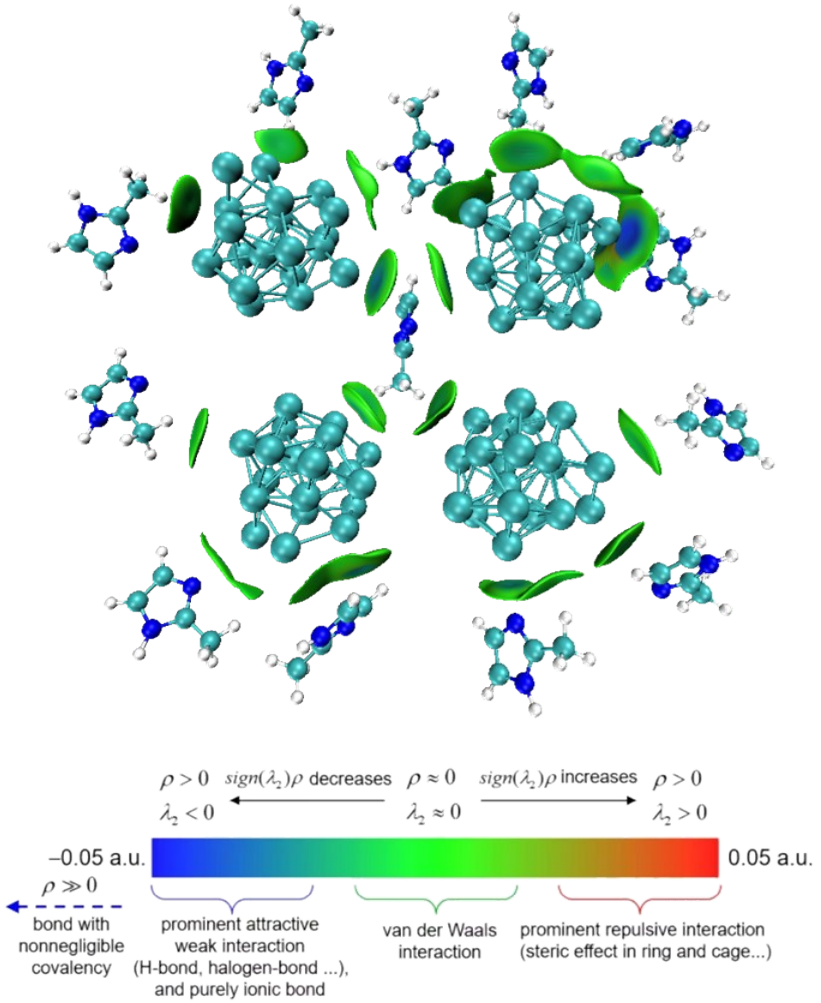

Figure S25. IGMH analysis of 2-methylimidazole-modified Cu NP tetramer.

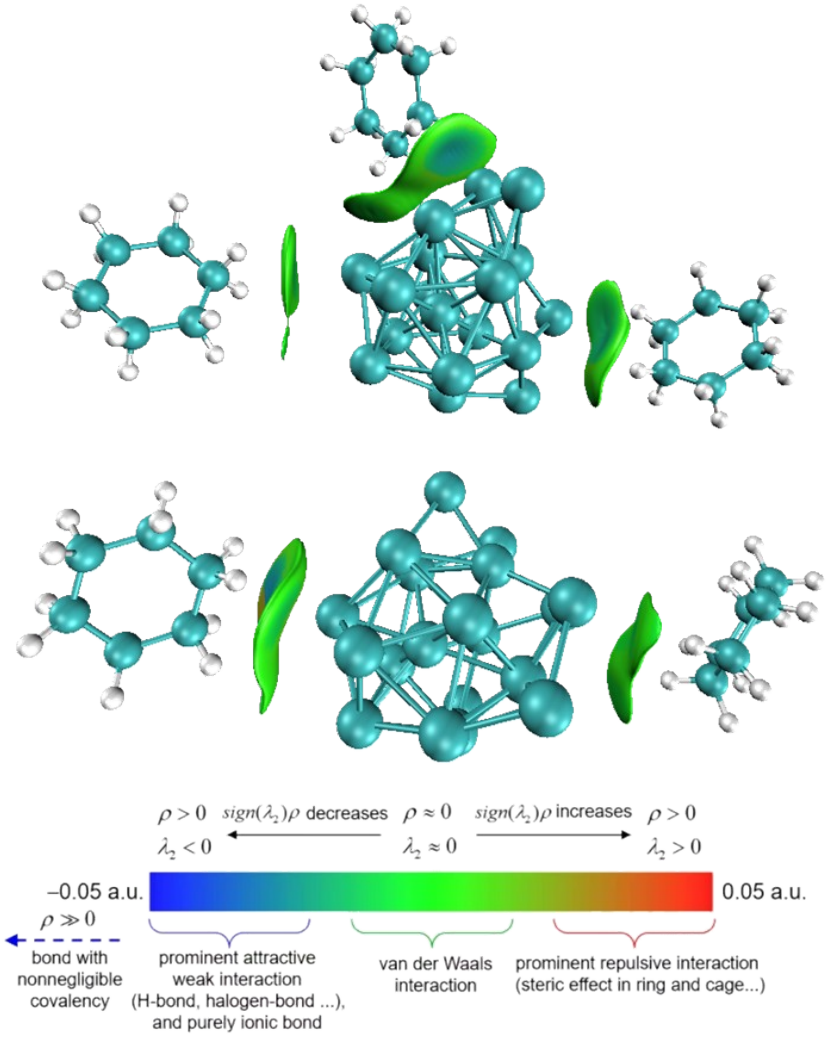

Figure S26. IGMH analysis of cyclohexane-modified Cu NP dimer.

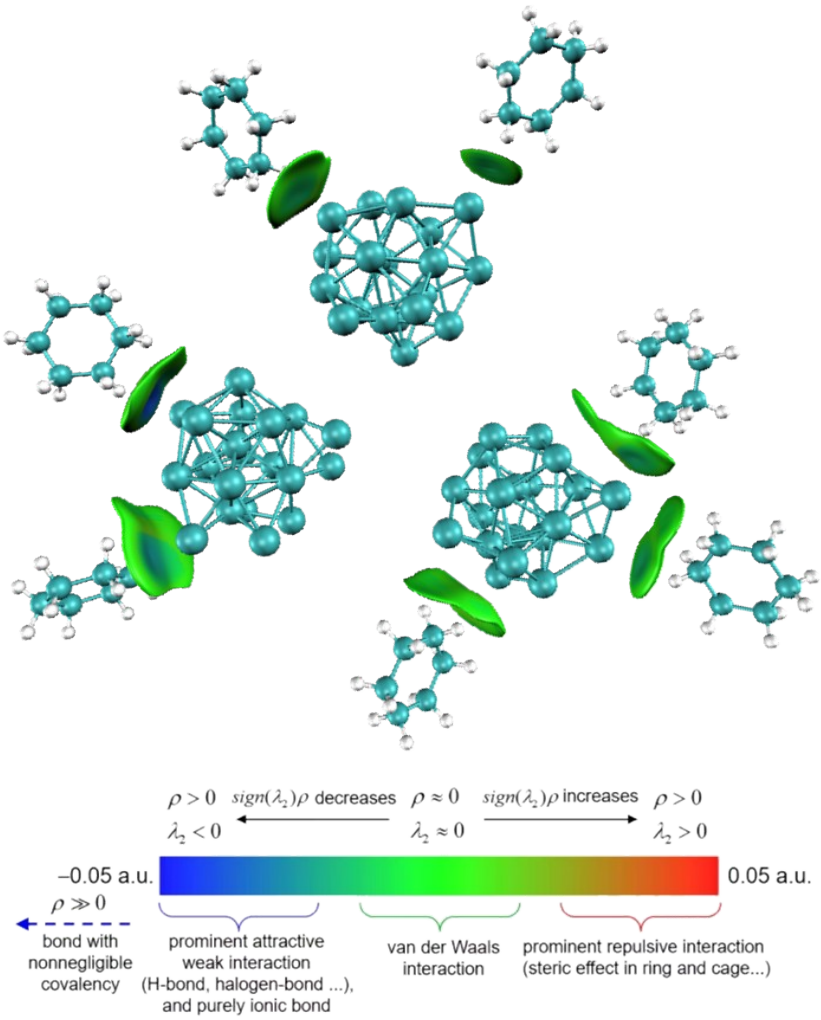

Figure S27. IGMH analysis of cyclohexane-modified Cu NP trimer.

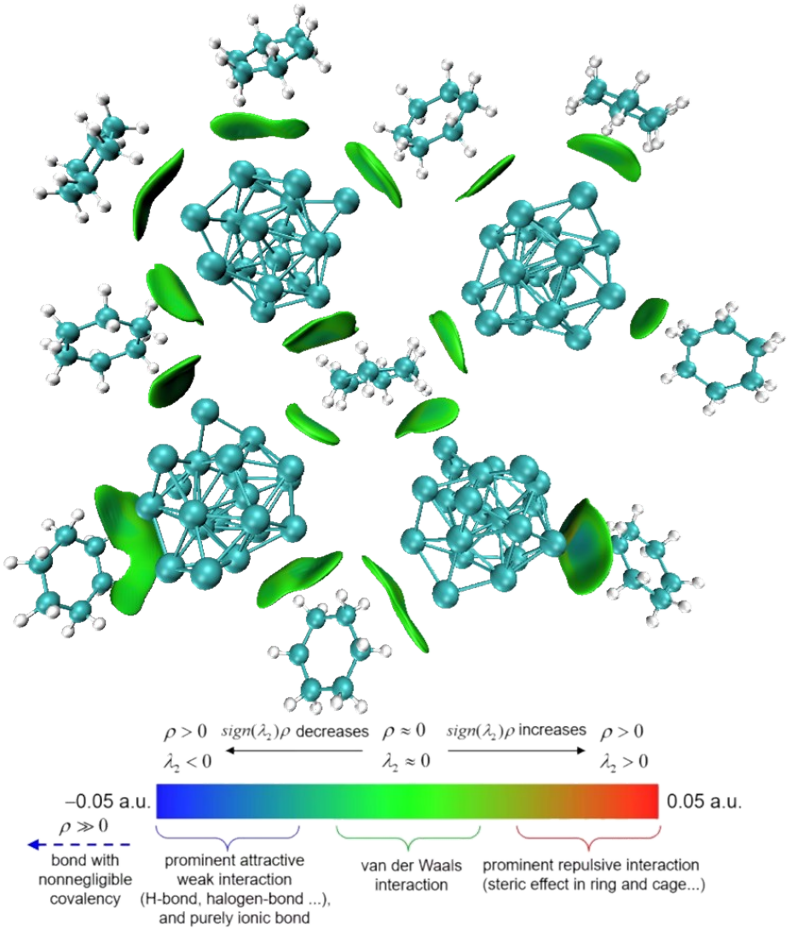

Figure S28. IGMH analysis of cyclohexane-modified Cu NP tetramer.

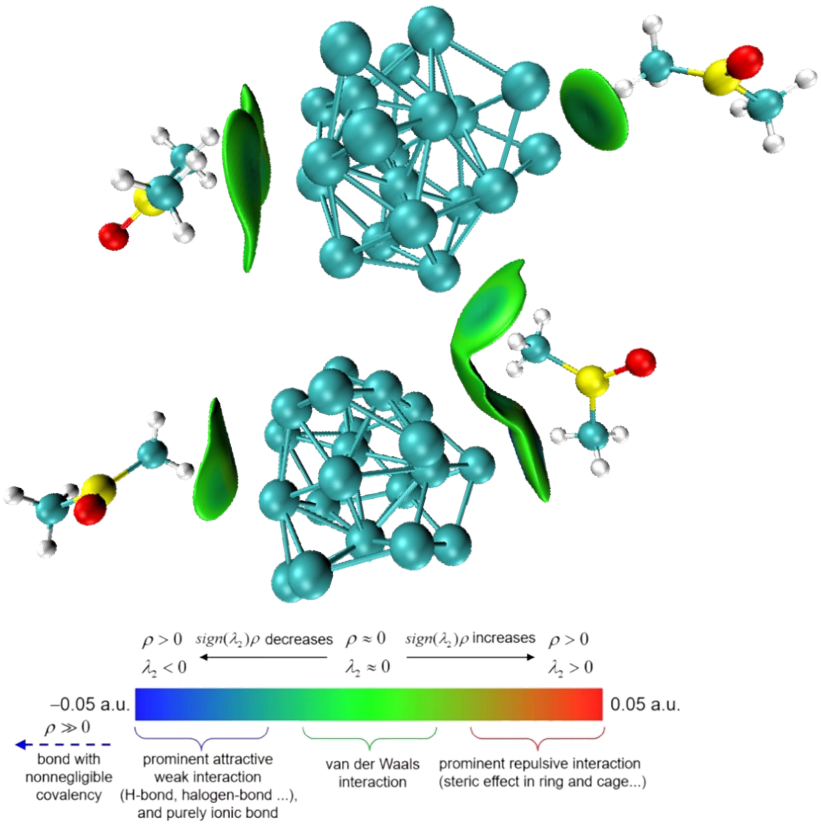

Figure S29. IGMH analysis of dimethyl sulfoxide-modified Cu NP dimer.

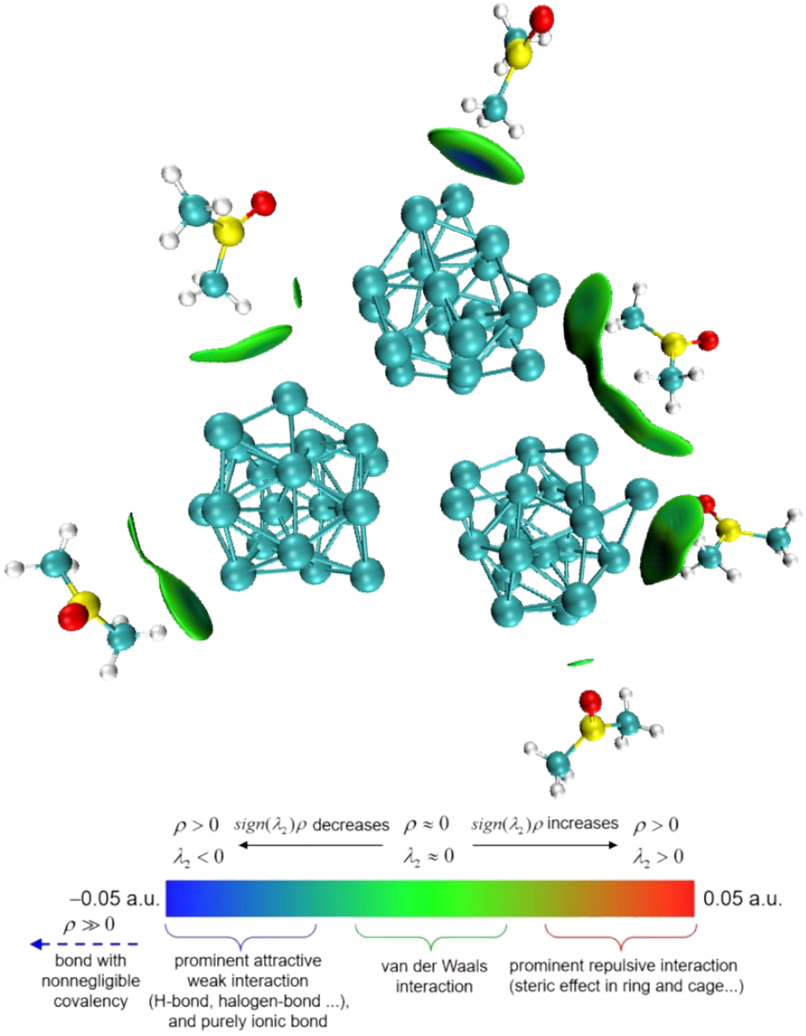

Figure S30. IGMH analysis of dimethyl sulfoxide-modified Cu NP trimer.

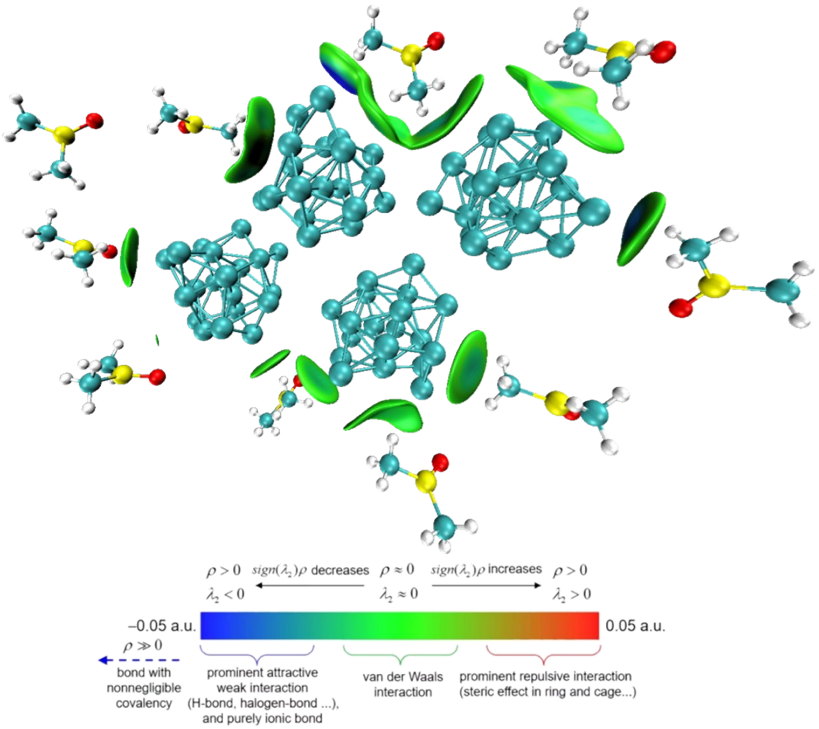

Figure S31. IGMH analysis of dimethyl sulfoxide-modified Cu NP tetramer.

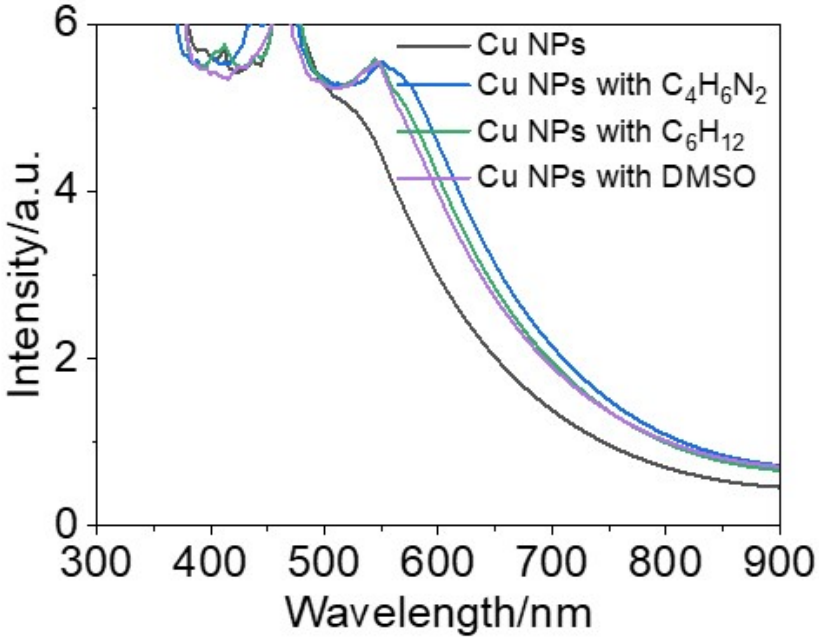

Figure S32. UV-vis absorption spectra of Cu NP aggregates and Cu NP aggregates after adding different compounds (2-methylimidazole, cyclohexane and dimethyl sulfoxide).

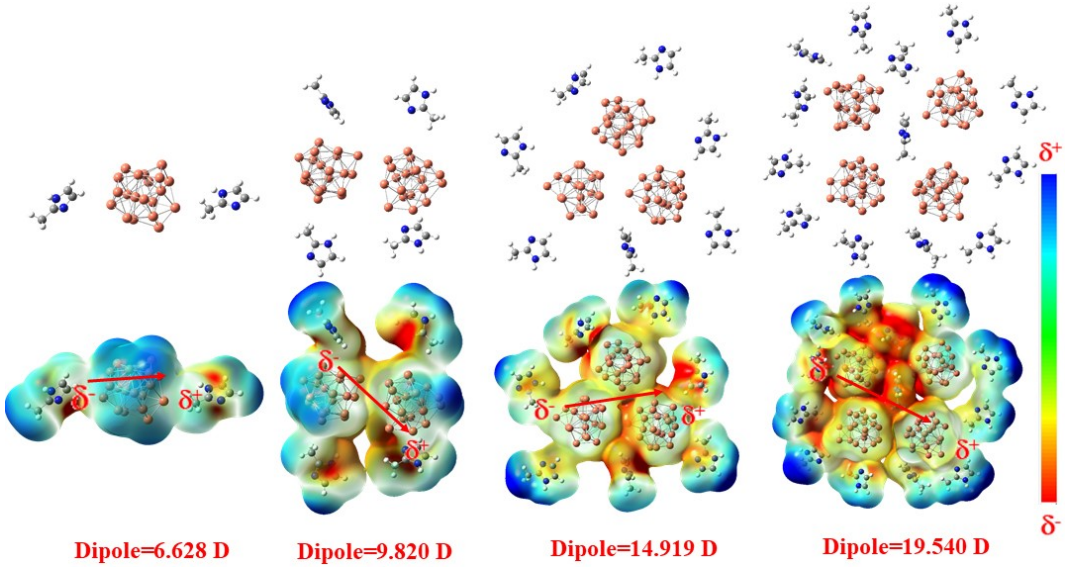

Figure S33. The dipole moment values and electrostatic potential distribution were calculated for 2-methylimidazole-modified Cu NPs with different degrees of aggregation.

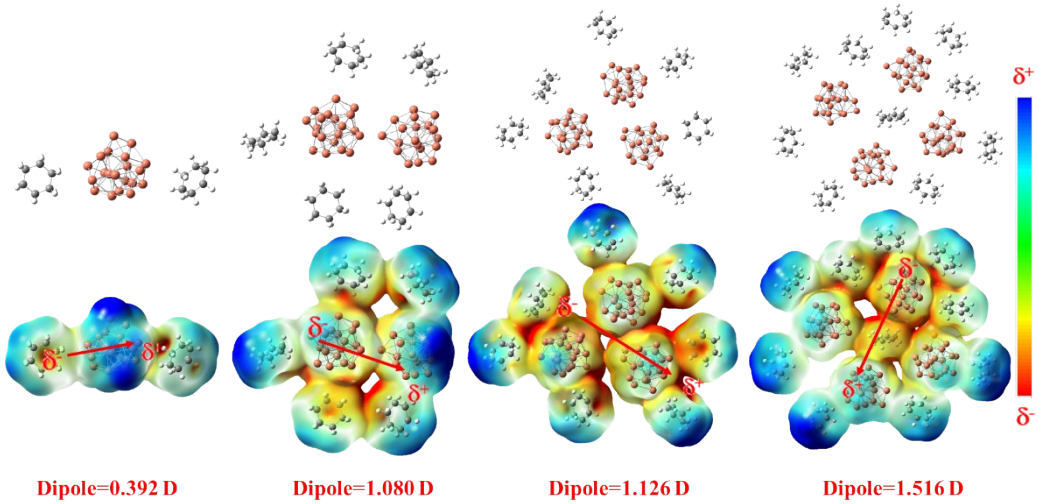

Figure S34. The dipole moment values and electrostatic potential distribution were calculated for cyclohexane-modified Cu NPs with different degrees of aggregation.

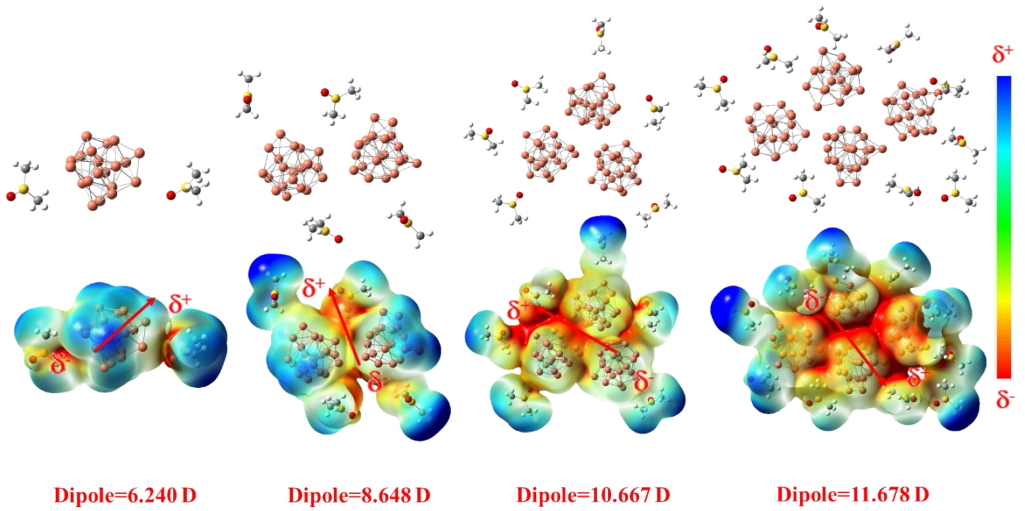

Figure S35. The dipole moment values and electrostatic potential distribution were calculated for dimethyl sulfoxide-modified Cu NPs with different degrees of aggregation.

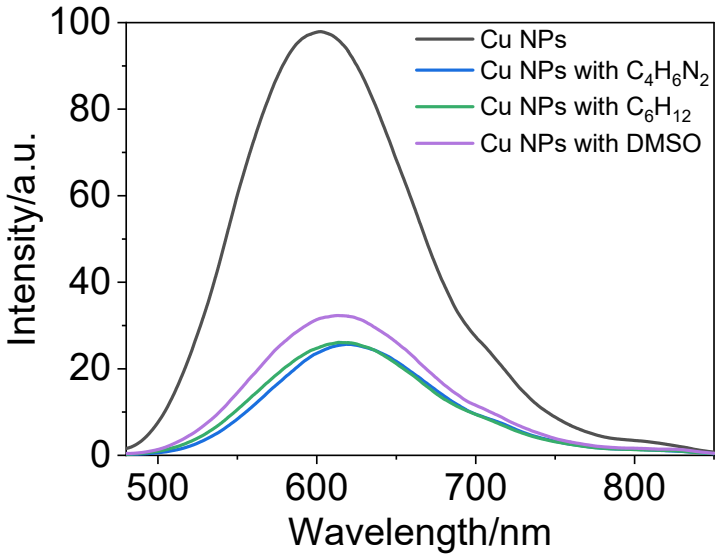

Figure S36. PL spectra of Cu NP aggregates and Cu NP aggregates after adding different compounds (2-methylimidazole, cyclohexane and dimethyl sulfoxide).

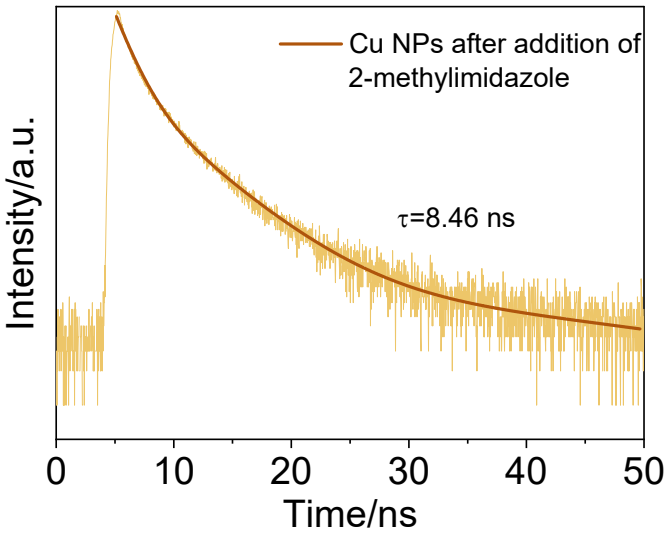

Figure S37. The PL lifetime of Cu NP aggregates after addition of 2-methylimidazole.

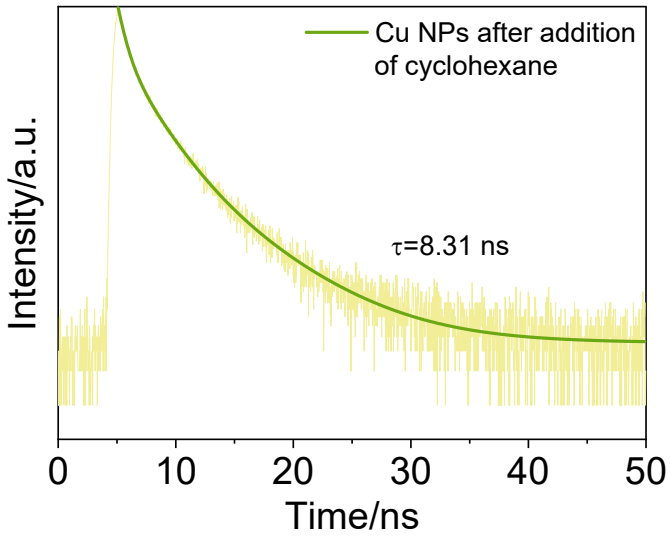

Figure S38. The PL lifetime of Cu NP aggregates after addition of cyclohexane.

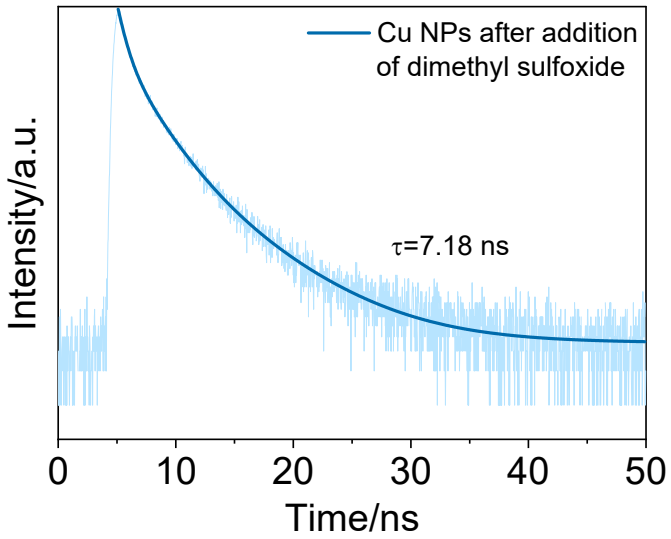

Figure S39. The PL lifetime of Cu NP aggregates after addition of dimethyl sulfoxide.

	Distribution of electron-hole	The exciton binding energy
Dimer	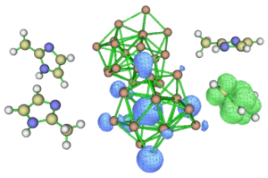	**1.21 eV**
Trimer	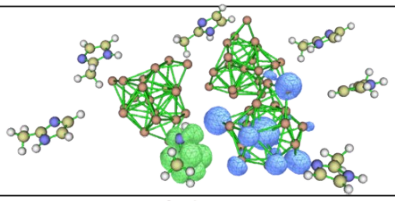	**1.04 eV**
Tetramer	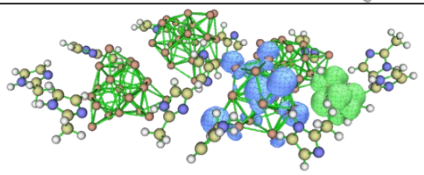	**0.75 eV**

Figure S40. Electron and hole distributions of S0 → S1 (green represents the electron distribution and blue represents the hole distribution) and the exciton binding energy were calculated for 2-methylimidazole-modified Cu NPs with different degrees of aggregation.

	Distribution of electron-hole	The exciton binding energy
Dimer	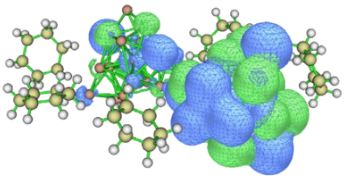	**1.25 eV**
Trimer	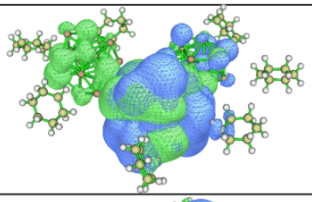	**1.13 eV**
Tetramer	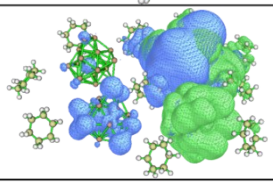	**0.84 eV**

Figure S41. Electron and hole distributions of S0 → S1 (green represents the electron distribution and blue represents the hole distribution) and the exciton binding energy were calculated for cyclohexane-modified Cu NPs with different degrees of aggregation.

	Distribution of electron-hole	The exciton binding energy
Dimer	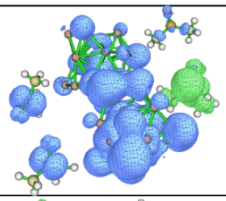	**1.33 eV**
Trimer	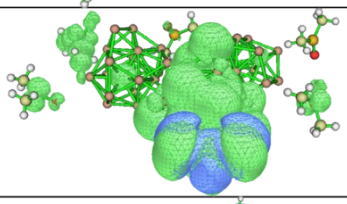	**1.20 eV**
Tetramer	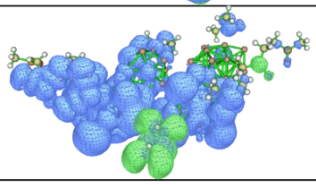	**0.80 eV**

Figure S42. Electron and hole distributions of S0 → S1 (green represents the electron distribution and blue represents the hole distribution) and the exciton binding energy were calculated for dimethyl sulfoxide-modified Cu NPs with different degrees of aggregation.

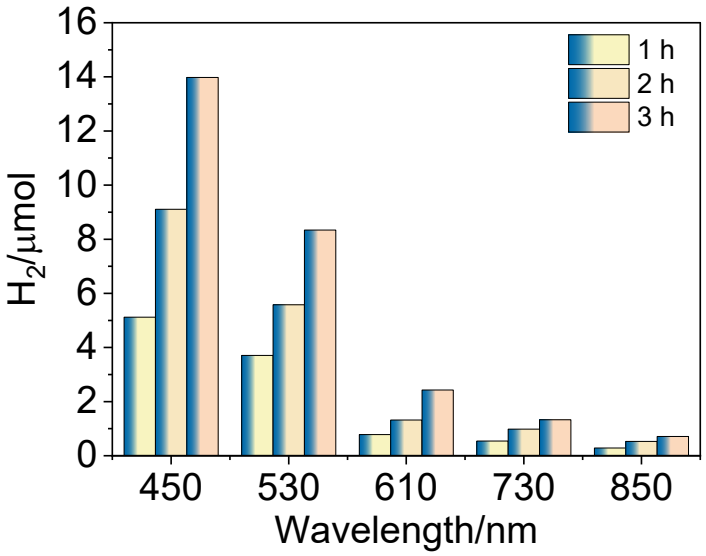

Figure S43. The photocatalytic performance of 2-methylimidazole-modified Cu NPs (0.6 mg/mL) under visible, red, and NIR light irradiation.

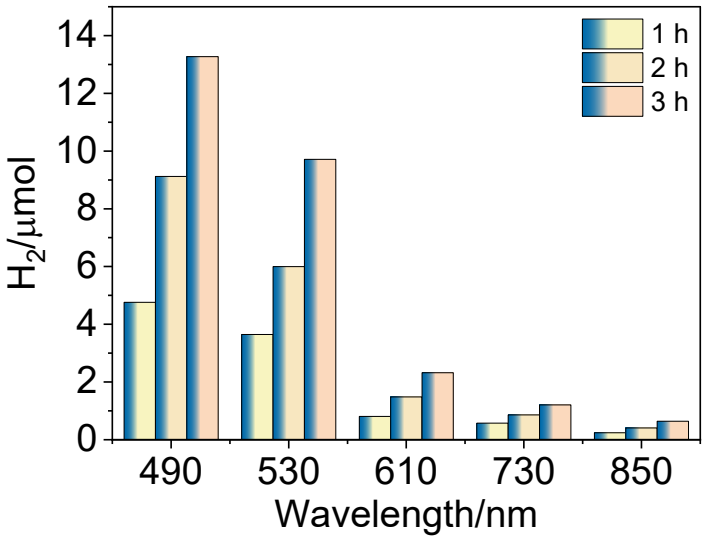

Figure S44. The photocatalytic performance of cyclohexane-modified Cu NPs (0.6 mg/mL) under visible, red, and NIR light irradiation.

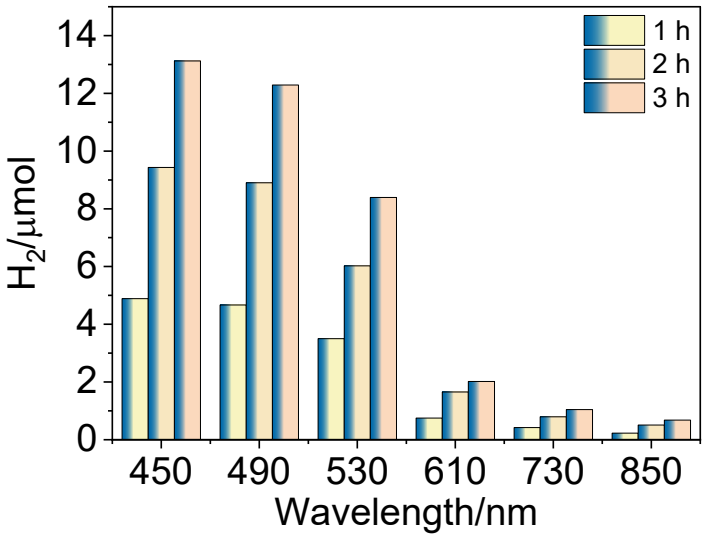

Figure S45. The photocatalytic performance of dimethyl sulfoxide-modified Cu NPs (0.6 mg/mL) under visible, red, and NIR light irradiation.

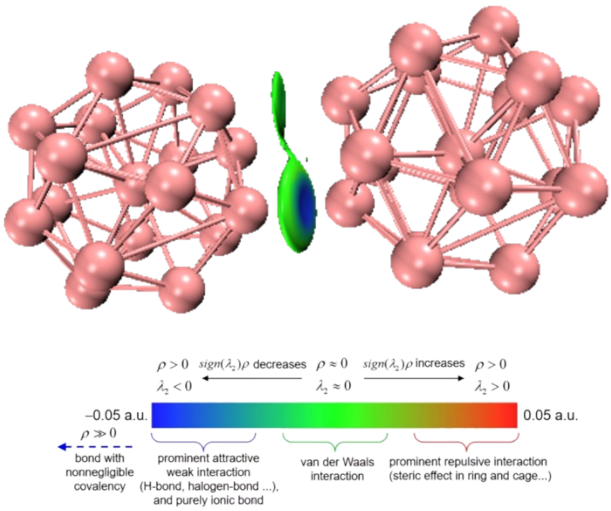

Figure S46. IGMH analysis of Ag NP dimer.

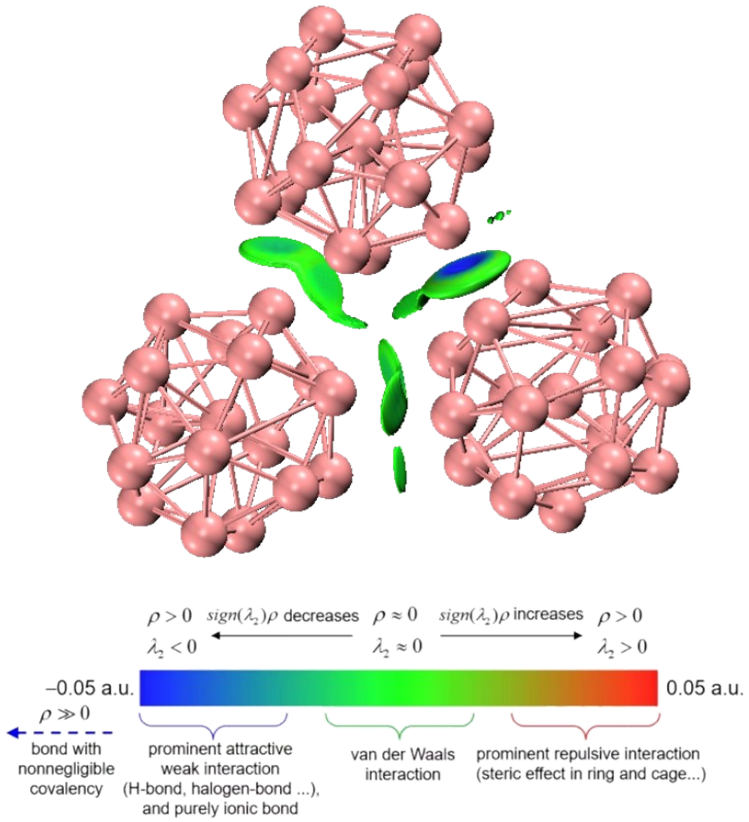

Figure S47. IGMH analysis of Ag NP trimer.

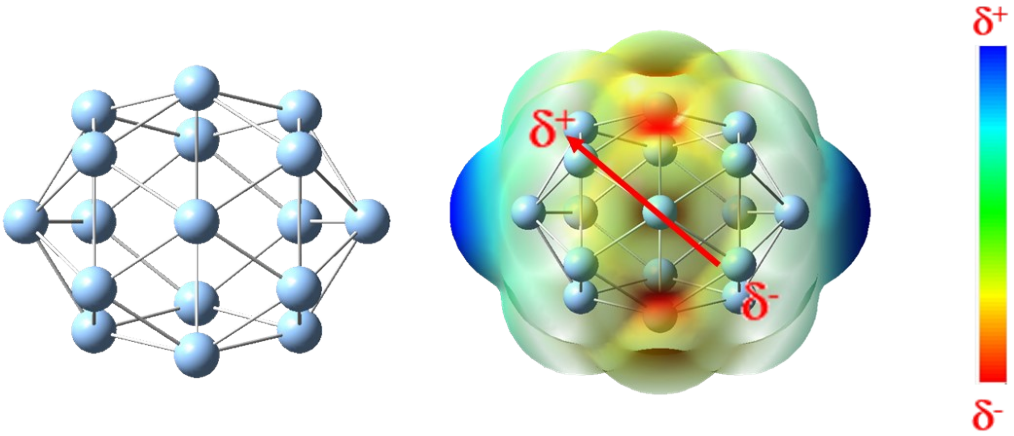

Figure S48. Electrostatic potential distribution of Ag NP monomer.

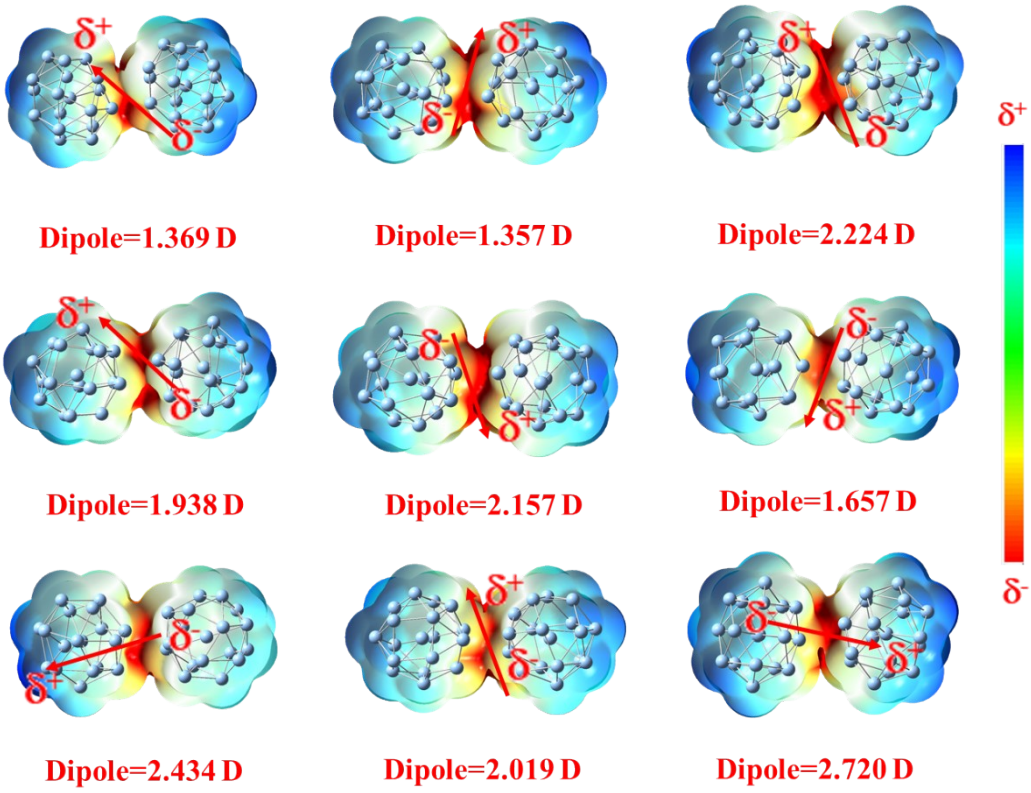

Figure S49. The dipole moments and electrostatic potential distribution were calculated for Ag NP dimers with different structures.

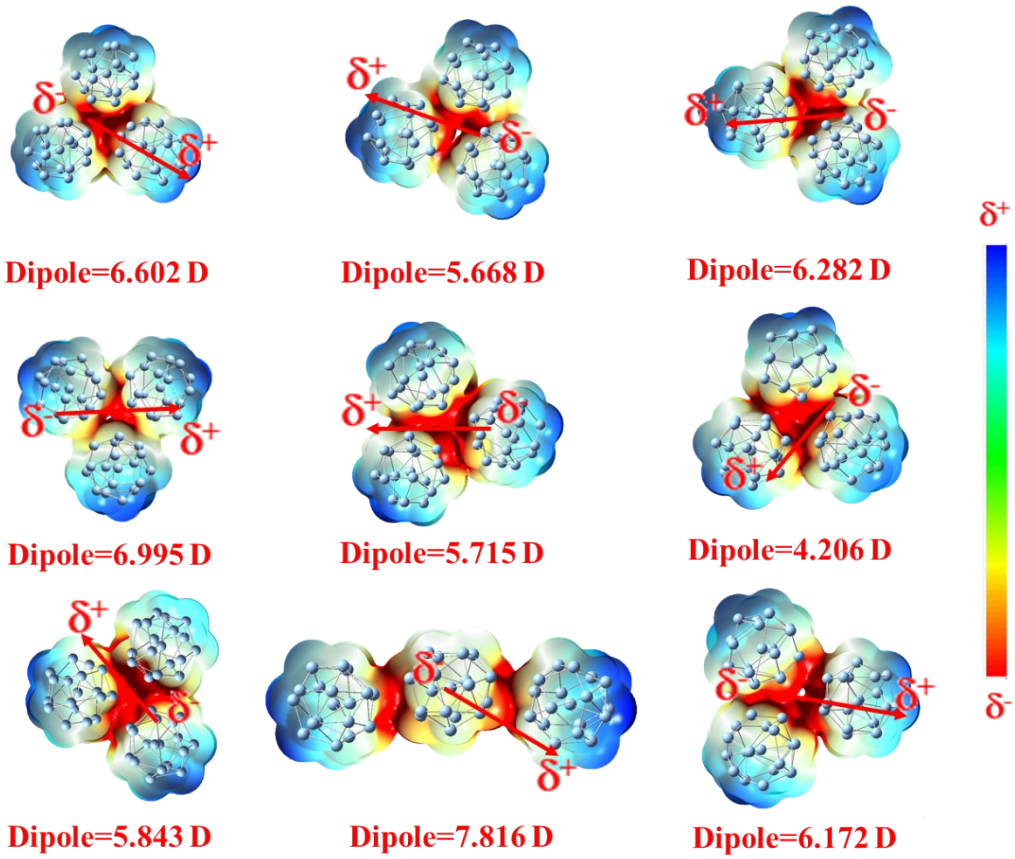

Figure S50. The dipole moments and electrostatic potential distribution were calculated for Ag NP trimers with different structures.

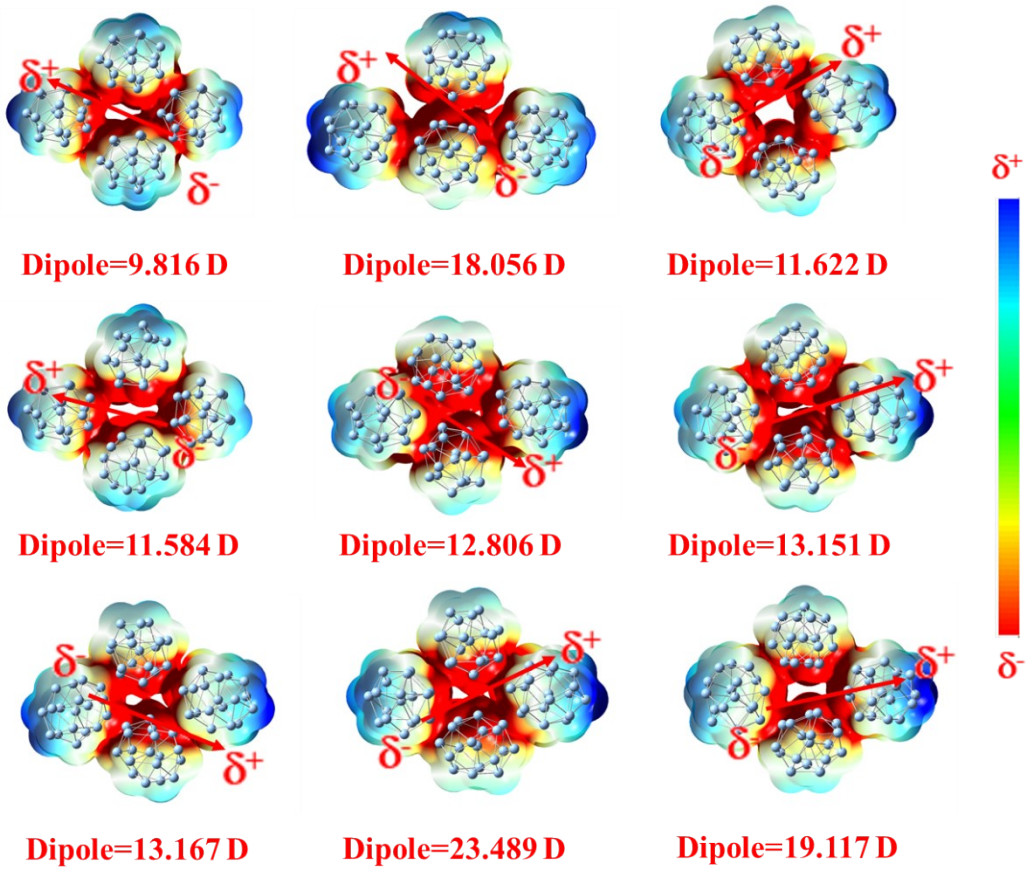

Figure S51. The dipole moments and electrostatic potential distribution were calculated for Ag NP tetramers with different structures.

	Distribution of electron-hole	The exciton binding energy
Monomer	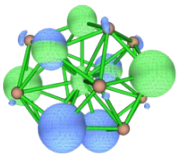	**3.89 eV**
Dimer	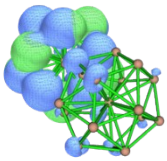	**3.40 eV**
Trimer	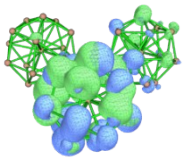	**2.61 eV**
Tetramer	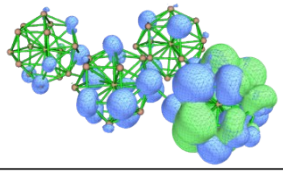	**2.30 eV**

Figure S52. Electron and hole distributions of S0 → S1 (green represents the electron distribution and blue represents the hole distribution) and the exciton binding energy were calculated for the different Ag NP aggregates.

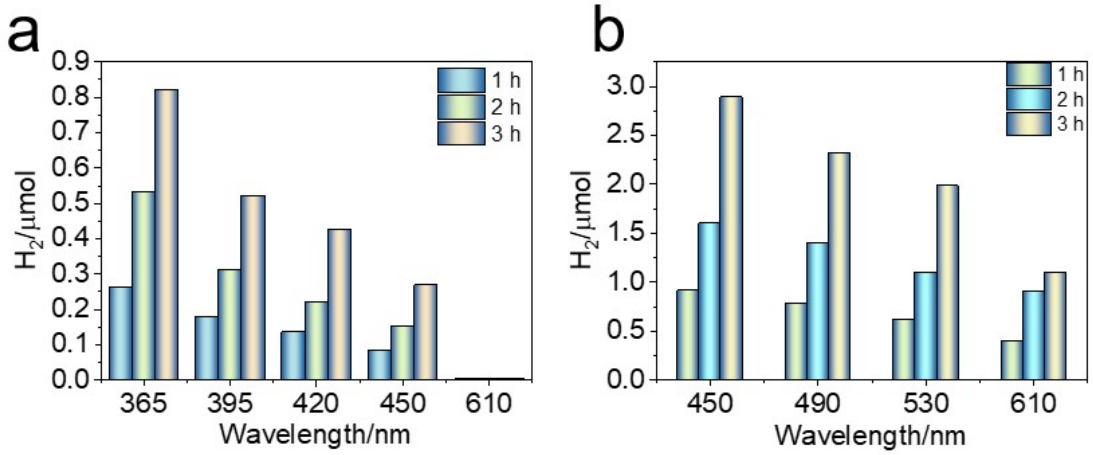

Figure S53. (a) The photocatalytic performance of Ag NPs (0.002 mg/mL). (b) The photocatalytic performance of Ag NPs (0.02 mg/mL).

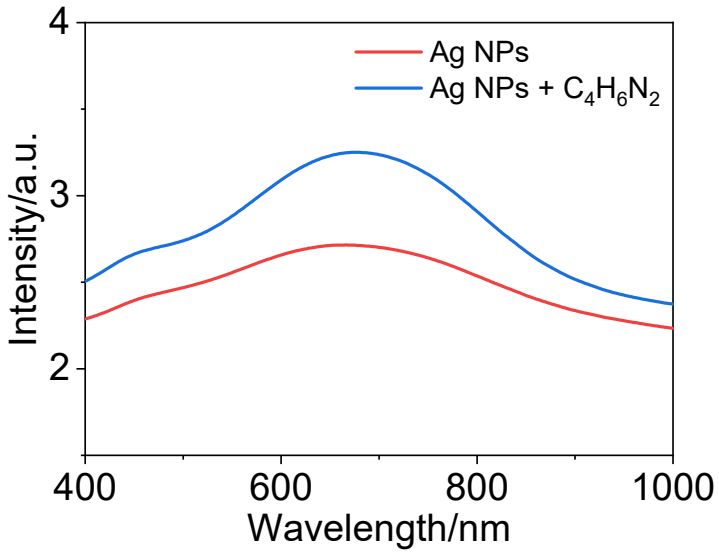

Figure S54. UV-vis absorption spectra of Ag NP aggregates and Ag NP aggregates with 2-methylimidazole modification.

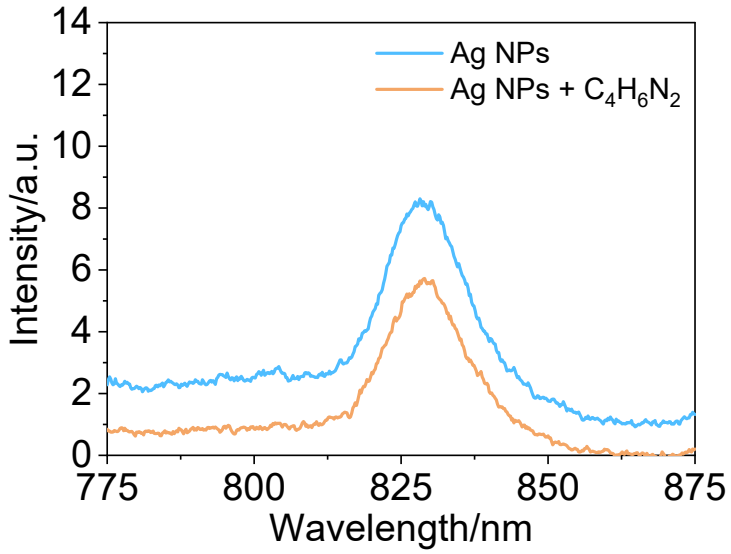

Figure S55. PL spectra of Ag NP aggregates and Ag NP aggregates with 2-methylimidazole modification.

Table S1. Key parameters of all LED light sources: wavelength, light intensity, and photon flux.

Wavelength (nm)	Light intensity (mW/cm^2)	Photon flux ($photons/(s \cdot cm^2)$)
365	45.12	8.28×10^{16}
395	42.02	8.35×10^{16}
420	39.51	8.35×10^{16}
450	41.65	9.43×10^{16}
490	40.85	1.01×10^{17}
530	46.97	1.25×10^{17}
610	20.36	6.25×10^{16}
850	31.41	1.34×10^{17}

Table S2. PL lifetimes of Cu NP monomer and Cu NP aggregates.

Samples	τ_1/ns	τ_2/ns	τ_3/ns	τ_{ave}/ns
Cu NP monomer	1.49001 (66.08%)	3.9290 (32.03%)	10.0623 (1.89%)	1.52
Cu NP aggregates	1.0001 (59.39%)	4.7020 (35.31%)	13.9985 (5.30%)	3.79
Cu NPs/H_3BO_3	10.410 (20.04%)	0.507 (79.81%)	22.9847 (0.15%)	9.23

Note: $\tau_{ave}=A_1*\tau_1^2+A_2*\tau_2^2+A_3*\tau_3^2/A_1*\tau_1+A_2*\tau_2+A_3*\tau_3$

Table S3. *f*s-TA kinetic parameters of Cu NP monomer and Cu NP aggregates.

Probe Wavelength/nm	τ_1/ps	τ_2/ps	τ_3/ps	τ_{ave}/ns
513 (Cu NP monomer)	0.14373 (33.85%)	0.14374 (33.76%)	0.14369 (32.4%)	0.01545
513 (Cu NP aggregates)	1.358 (50.76%)	11.219 (36.86%)	101.739 (12.38%)	1.47
570 (Cu NP aggregates)	1.678 (59.97%)	14.813 (29.99%)	129.728 (10.04%)	2.48

Note: $\tau_{ave}=A_1*\tau_1^2+A_2*\tau_2^2+A_3*\tau_3^2/A_1*\tau_1+A_2*\tau_2+A_3*\tau_3$

Table S4. Comparison of hydrogen photosynthesis activities with state-of-the-art plasmonic photocatalysts under red/NIR light irradiation.

Photocatalysts	Electron donors	AQY/%	Refs.
Au/PFC-9	TEOA	0.002939 (600 nm) 0.000782 (700 nm)	1
Ag@SiO_2@CdS-Au	Na_2S-Na_2SO_3	0.095(600 nm)	2
Au nanorods/$La_2Ti_2O_7$	Methanol	0.5(700 nm)	3
(Au/AgAu)@CdS	Na_2S-Na_2SO_3	0.23(500 nm)	4
AuCS@CdSs	Na_2S-Na_2SO_3	0.04(600 nm)	5
A(P)MC	Na_2S-Na_2SO3	0.26(520 nm)	6
M/W-15		0.15(600 nm)	7
Au NRs/TMC-780	Methanol	0.36(600 nm)	8
5-Au@Cu7S4	Methanol	0.8(600 nm)	9
G-AuONC@TiO2CSNs	Methanol	0.31(700 nm)	10
Cu NP aggregates	TEA	0.82(610 nm) 0.191(850 nm)	This work

Supplementary references

1. Q. Q. Huang, Z. B. Fang, K. Pang, W. K. Qin, T. F. Liu and R. Cao, *Adv. Funct. Mater.*, 2022, DOI: 10.1002/adfm.202205147.
2. H. Ren, J.-L. Yang, W.-M. Yang, H.-L. Zhong, J.-S. Lin, P. M. Radjenovic, L. Sun, H. Zhang, J. Xu, Z.-Q. Tian and J.-F. Li, *ACS Mater. Lett.*, 2020, **3**, 69-76.
3. X. Cai, M. Zhu, O. A. Elbanna, M. Fujitsuka, S. Kim, L. Mao, J. Zhang and T. Majima, *ACS. Catal.*, 2017, **8**, 122-131.
4. L. Ma, Y.-L. Chen, D.-J. Yang, H.-X. Li, S.-J. Ding, L. Xiong, P.-L. Qin and X.-B. Chen, *Nanoscale*, 2020, **12**, 4383-4392.
5. Z. Xu, W. Yue, C. Li, L. Wang, Y. Xu, Z. Ye and J. Zhang, *ACS Nano*, 2023, **17**, 11655-11664.
6. M. Ma, J. Liu, H. Zhao, S. Yue, L. Zhong, Y. Huang, X. Jia, K. Liu, X. Li, Z. Wang, S. Qu and Y. Lei, *Appl. Catal. B-Environ.*, 2023, DOI: 10.1016/j.apcatb.2022.122327.
7. Y. He, Y. Yang, C. R. Bowen, Z. Shu, L. Zheng, N. Tu, T. Lu, W. Li and W. Yang, *Chem. Eng. J.*, 2024, DOI: 10.1016/j.cej.2023.148299.
8. O. Elbanna, S. Kim, M. Fujitsuka and T. Majima, *Nano Energy*, 2017, **35**, 1-8.
9. C.-W. Tsao, S. Narra, J.-C. Kao, Y.-C. Lin, C.-Y. Chen, Y.-C. Chin, Z.-J. Huang, W.-H. Huang, C.-C. Huang, C.-W. Luo, J.-P. Chou, S. Ogata, M. Sone, M. H. Huang, T.-F. M. Chang, Y.-C. Lo, Y.-G. Lin, E. W.-G. Diau and Y.-J. Hsu, *Nat. Commun.*, 2024, DOI: 10.1038/s41467-023-44664-3.
10. H. Jung, J. Song, S. Lee, Y. W. Lee, D. H. Wi, B. S. Goo and S. W. Han, *J. Mater. Chem. A*, 2019, **7**, 15831-15840.